Universitat Politècnica de Catalunya
Electrical Engineering Department

Institut de Recerca en Energia de Catalunya
Catalonia Institute for Energy Research

Master Thesis

Modeling, control and experimental validation of a DFIG-based wind turbine test bench

Author: **Jonathan Fournier**

Advisors: **Francisco Díaz González**
Agustí Egea Alvarez

Barcelona, July 2013

Catalonia Institute for Energy Research (IREC)
Electrical Engineering Research Area
Jardins de les Dones de Negre 1 2nd floor,
08930 Sant Adrià de Besòs, Barcelona, Spain

Printed in Barcelona by CPET, S.L.
First Print, July 2013

To my brother Yannick

Abstract

The penetration of wind energy has been fast increasing during the last decade across the world. In order to maintain and improve this growth level, the EWEA introduced a wind research and development plan: the European Wind Initiative (EWI). It aims, among others, at making onshore and offshore power the most competitive energy source and reach wind energy penetration levels of 20% by 2020 and 50% by 2050 [7]. Because of this growing penetration and given the high variability of wind speed profiles and the consequent energy shortage, regulations have been established by the transmission system operators to define the parameters that must be met by power plants connected to the electric network such as ride-thru requirement and voltage regulation.

As mentioned in a EWEA report published in 2013 [6], one of the main advantages of wind energy is its ability to contribute to the system operation and flexibility. Indeed, a variable-speed turbine equipped with power converters has the ability to control the flow of reactive power and inject it into the grid in periods of voltage drop to contribute to voltage stabilization. The possibility to capture a greater amount of energy by adapting the turbine speed to the wind velocity is another important motivation behind the growing share of variable-speed turbines (VSWT).

Among the different VSWT topologies, the DFIG system is of special interest given its high energy efficiency and controllability but especially because of the low power rating - and lower cost - of its power converters

that only need to process one third of the rated turbine power [22]. Several different control methods exist to control the active and reactive power flows through these converters. Some of these algorithms will be presented in this report and implemented both in a software simulation and on a wind turbine test bench.

Acknowledgements

This thesis has been supported by Catalonia Institute for Energy Research (IREC) and KIC InnoEnergy. I especially want to thank:

- My supervisor Francisco for the precious and patient support, experienced tips and thorough review. Agusti Egea for giving me the drive to learn more in the great field of wind power.

- My parents, my brother and my friends for their support and understanding through demanding studies and work.

- François, Gingras, Jean-François, Pelland, Benjamin, Mélanie, Pascal.

- All the Selecters who kept the passion for renewable energy alive. Specially Manolo and Jose who struggled with me through thesis writing.

Contents

List of Tables

List of Figures

Glossary

Abbreviations

Name	Description
VSC	Voltage Source Converter
FRT	Fault Ride-Through
LCC	Line-Commutated Converter
VCO	Voltage-Controlled Oscillator
PLL	Phase-Locked Loop
IGBT	Insulated-Gate Bipolar Transistor
VSWT	Variable Speed Wind Turbine
WTGS	Wind Turbine Generation System

Mechanical variables

Name	Description	Unit
c_1 to c_9	Power factor coefficients	-
C_p	Coefficient of power	-
J_t	Turbine inertia	kg m^2
J_g	Generator inertia	kg m^2
R	Turbine blade radius	m
v_w	Wind speed	m/s
T_g	Electrical generator torque	Nm
T_t	Mechanical turbine torque	Nm
β	Pitch angle	degrees

Electrical variables and parameters

Name	Description	Unit
ω_e	Grid frequency	rad/s
ω_{sync}	Synchronous frequency	rad/s
ω_{rotor}	Rotor frequency (= generator speed * P_p)	rad/s
ω_{slip}	Slip frequency	rad/s
λ_{qs}	Q-axis stator flux	Wb trn/s
λ_{ds}	D-axis stator flux	Wb trn/s
λ_{qr}	Q-axis rotor flux	Wb trn/s
λ_{dr}	D-axis rotor flux	Wb trn/s
V_{qs}	Q-axis stator voltage	V
V_{ds}	D-axis stator voltage	V
$V_{qr}^{'}$	Q-axis rotor voltage wrt stator	V
$V_{dr}^{'}$	D-axis rotor voltage wrt stator	V
i_{qs}	Q-axis stator current	A
i_{ds}	D-axis stator current	A
$i_{qr}^{'}$	Q-axis rotor current wrt stator	A
$i_{dr}^{'}$	D-axis rotor current wrt stator	A
υ_z	Grid voltage	V
υ_{cz}	Voltage at GSC terminals	V
Z_{eq}	Equivalent impedance of GSC	Ω
R_{eq}	Equivalent resistance of GSC	R
L_{eq}	Equivalent inductance of GSC	H
δ	Alignment angle for control reference frame	rad
C_{DC}	DC link capacitance	rad/s
P_p	Generator pole pair	rad/s
L_m	Magnetizing inductance	H
L_{ls}	Stator leakage inductance	H
L_{lr}	Rotor leakage inductance	H
X_m	Magnetizing reactance	Ω
X_{ls}	Stator winding leakage reactance	Ω
X_{lr}	Rotor winding leakage reactance (wrt stator)	Ω
X_s	Stator reactance	Ω
X_r	Rotor reactance	Ω
R_r	Rotor winding resistance	Ω
R_s	Stator winding resistance	Ω

1 Introduction

This project, performed with the Catalonia Institute for Research Energy (IREC) comes from the will to install and commission a DFIG wind turbine test bench for further experimentations. The system analyzed in the computer simulation mimics the characteristics of the test bench, with the objecitve of comparing theoretical and experimental results.

In the first stage, a wind generation system is modelled and simulated through Matlab/Simulink. This model consists of a doubly-fed induction generator (DFIG) coupled to a horizontal-axis wind turbine and a back-to-back power converter that regulates the voltage applied to the rotor windings. In order to reduce the simulation time, the simulation was not designed to represent a high level of realism such as the IGBT switching. Two control approaches were simulated for the rotor-side converter, featuring two different control variable orientation. Once the simulation results proves satisfying, the controls are implemented on the converter-mounted digital signal processors (DSPs) of a test bench.

Chapter two presents the different wind turbine types, the specific characteristics of a DFIG generator and the characteristics of power converters. Chapter three describes the models and equations used to represent the system components in simulation. Chapter four describes the control algorithms for the rotor-side, the grid-side converters and an sensorless method to obtain the rotor angle. Finally, chapter five discusses the experimental results and complications resulting from the implementation of the controls on a test bench.

2

DFIG and power converter characteristics

In this section, the advantages of a variable speed turbine are explained and the overall arrangement of a wind turbine generation system using a doubly-fed induction generator is described.

2.1 Variable vs fixed speed wind turbines

Fixed-speed wind turbines were widely installed in the past because of their simplicity and low cost. However, their design requires a direct grid connection that keeps their speed constant, generates strong power and torque fluctuations and allows maximal efficiency only at the nominal wind speed. Varying the turbine speed offers the possibility to adapt the turbine speed to the wind speed and operate at optimal aerodynamic efficiency in the design region. In VSWT, the electromagnetical torque is usually controlled to follow the optimal aerodynamic Betz coefficient (Cp) in the turbine's partial load region. This allows achieving maximal energy conversion efficiency over a wide array of wind speeds, reducing the mechanical stress and injecting higher quality power in the grid [23]. Figure 2.1 shows the different system operating modes. Below the cut-in and above the cut-out speed, the turbine is not operated. The operating zone is divided in three sections:

- Design zone (I): The wind speed is between V_{cut-in} and V_{nom}, the VST control system aims at optimizing the efficiency of the conversion from

the wind kinetic energy to mechanical energy. This region is also called the Partial Load Region.

- Transition zone (II): The wind speed is between V_{nom} and the wind speed providing P_{nom}. The control objective is the same as in region I.
- Nominal power zone (III): The wind speed is between V_{nom} and $V_{cut-out}$, the high level control adjusts the blade pitch angle to limit the transmitted torque and maintain the power at its rated value.

The prevalent control algorithm in operating zone III modifies the wind turbine aerodynamic properties to limit the output power. However, on the test bench used in the present study, the aerodynamic generator is replaced by an induction motor emulating the WT fast-axis shaft rotation. Thus, since the pitch angle control cannot be experimentally implemented, it has been left out of simulation and wind speed input is limited to the speed at $P_{nominal}$.

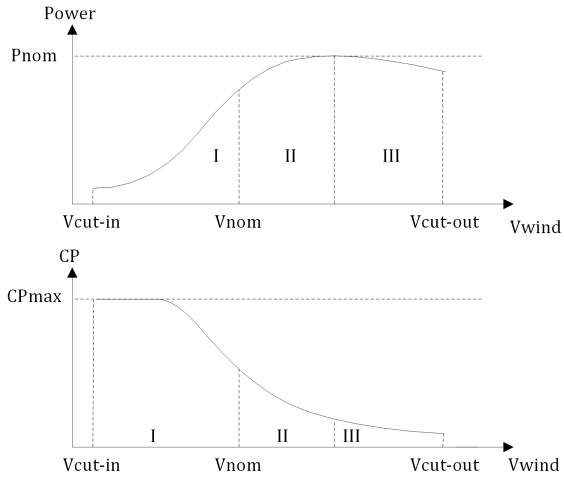

Figure 2.1: Power and coefficient of power of variable speed wind turbine

2.2 Doubly fed induction generator (DFIG) system

The doubly-fed induction generator (DFIG) is one type of VSWT configurations whose share in the wind turbine installation has been growing during

the last years. Doubly-fed induction generator is a common drive system for large motors requiring limited variable speed applications. The shaft speed is varied by controlling the amount of power transferred to the rotor through a bi-directional voltage-source back-to-back (B2B) power converter that features very high speed switching performed by IGBTs (Figure 2.2). In wind turbine applications the system still requires a gearbox to accelerate the turbine rotation into the generator.

The main advantage of the DFIG system over SCIG generators is the capability to perform fault ride-thru and reactive power control. Furthermore, since the power converters only process the rotor circuit power — typically 20 to 30% of rated turbine power — their size and cost is considerably smaller than in full power conversion systems, where all the turbine power is processed by the converter. These assets make the DFIG a design of choice from the point of view of the grid operators. Its ability to assists the grid in voltage control is especially sought after now that renewable energy penetration is on the rise worldwide.

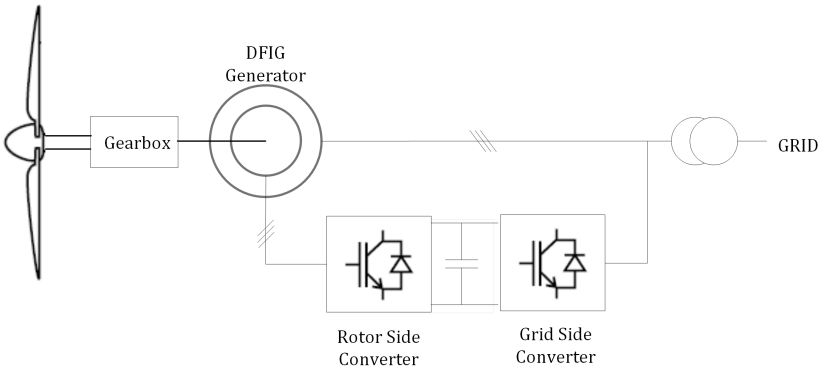

Figure 2.2: DFIG wind turbine system layout

2.3 Power converters

Power electronic is increasingly used nowadays in distributed energy system. Bi-directional AC-DC power converters offer the possibility to control the flows of active and reactive power and therefore, are an asset when voltage or frequency compensation and fault ride-through (FRT) are required by the transmission system operator. The main types of converters used nowadays

for these applications are line-commutated converters (LCC) and voltage-source converter (VSC). The latter uses IGBTs as the switching device and is often preferred given its black-start capability and its supply of low harmonic current. At low voltage levels, a two-level converter is commonly used while multi-level technologies can be used for higher voltage applications.

The back-to-back converter is used to control the power flow in the rotor circuit. Since the turbine needs to be operated in both super-synchronous and sub-synchronous modes, the rotor current must be allowed to circulate in both directions. Hence, both converters are used in alternance as rectifiers and as inverters. They are connected together through a DC bus bar, whose voltage must be kept constant. Sections 4.2 and 4.3 expose the control algorithm of the rotor-side-converter and the grid-side-converter.

3 Modeling of the DFIG wind turbine

This section presents the optimal methods used in software simulation of the turbine sub-systems: turbine, transmission, generator and converters. Since the test bench is not a perfect representation of a real WT, some simplifications are brought to the simulation in order to allow comparison between theoretical results and practical ones.

3.1 Turbine modeling

The wind turbine blades convert the wind energy into mechanical energy in the form of a rotating shaft. The maximal amount of energy that can be transferred in this manner is set by the Betz limit. Equation (3.1) [1] represents the energy that can be captured by the blades.

$$P_{rotor}^{Max} = C_p \frac{1}{2} \rho A v_{wind}^3 \tag{3.1}$$

Where C_p is the coefficient of power, also called Betz coefficient. It represents the ratio between the energy that can be extracted by the blades and the available wind kinetic energy. Since the wind speed after the wind turbine still has a non-zero speed, all the energy is not transfered to the blades. In equation (3.2) obtained by applying the Bernoulli equation through the turbine, v_1 and v_2 are the wind speed upstream and downstream from the turbine respectively.

$$P_{rotor} = \rho A \frac{v_1 + v_2}{2} \left(\frac{v_1^2}{2} - \frac{v_2^2}{2} \right) \tag{3.2}$$

By stating that $k = v_2/v_1$, it can be re-arranged in the following way:

$$P_{rotor} = \frac{1}{2} \rho A v_{wind}^3 \cdot \frac{1}{2}(1+k)(1-k^2) \tag{3.3}$$

This equation is maximized when $k = 1/3$, which leads to an optimal coefficient of power of $C_p^{max} = 0.59$. This coefficient is characteristic to each turbine and can be determined from the parameters c_1 to c_9:

$$CP(\lambda, \beta) = c_1 \left(c_2 \frac{1}{\Lambda} - c_3 \beta - c_4 \beta^{c_5} - c_6 \right) e^{-c_7 \frac{1}{\Lambda}} \tag{3.4}$$

Where λ= Tip speed ratio = $\omega_t R / v_{wind}$.

The power coefficient depends on the tip speed ratio λ and on the blade pitch angle. Its optimization is the key difference between fix speed and variable speed turbines and will be one objective of the control algorithm.

3.2 Transmission system modeling

The wind turbine transmisison is represented by a one-mass system, described by equation 3.5 and Figure 3.1. The inertia of the components rotating on the slow-axis is gathered under the term J_t while the generator inertia is represented by J_g. The torques acting on the rotating components are the generator electrical torque T_g and the torque applied by the wind on the blades T_t.

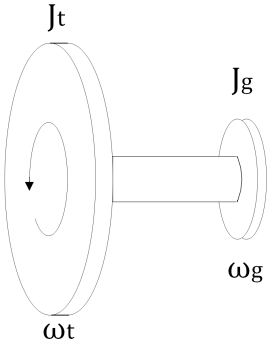

Figure 3.1: One mass model

$$T_g - T_t^{'} = (J_t^{'} + J_g)\frac{d\omega_g}{dt} \tag{3.5}$$

Where: $T_t^{'}= T_t/n$, $J_t^{'}= J_t/n^2$ and n is the ratio of the gearbox linking the fast-axis and slow-axis systems.

3.3 Generator modeling

An induction machine works on the principle of the interraction between the stator and rotor magnetomotive forces (MMF). The stator winding currents create a MMF rotating at grid frequency that induces a MMF in the rotor windings if the rotor speed does not match the stator's MMF. This induced rotor MMF will rotate at the so-called slip frequency which has the following value:

$$\omega_{slip} = \omega_{MMF}^{rotor} = \omega_{MMF}^{stator} - \omega_{rotor} \tag{3.6}$$

Where:

- ω_{slip} is the slip frequency, corresponding to the frequency of rotor current and voltage
- ω_{MMF}^{stator} is the frequency of the stator MMF, corresponding to the grid frequency
- ω_{rotor} is the rotor rotating frequency, equal to the mechanical frequency multiplied by the number of pole pairs

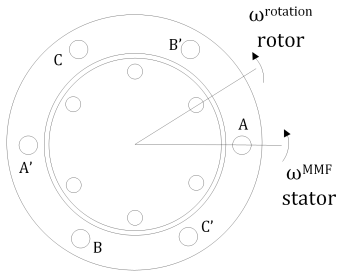

Figure 3.2: Induction machine winding layout

For simulation purposes, it is assumed that both sides are connected in Y with the neutral being at zero voltage and have the same number of turns (Turn Ratio=1). The following are the basic equations guiding the DFIG generator behavior [23]:

$$\begin{aligned} \upsilon_s^{abc}(t) &= R_s^{abc}(t) i_s^{abc}(t) + \frac{d\lambda_s^{abc}(t)}{dt} \\ \upsilon_r^{abc}(t) &= R_s^{abc}(t) i_r^{abc}(t) + \frac{d\lambda_r^{abc}(t)}{dt} \end{aligned} \tag{3.7}$$

$$\begin{aligned} \lambda_s^{abc}(t) &= L_s i_s^{abc}(t) + L_m i_r^{abc}(t) \\ \lambda_r^{abc}(t) &= L_r i_r^{abc}(t) + L_m i_s^{abc}(t) \end{aligned} \tag{3.8}$$

Where

- L_m = magnetizing inductance
- L_s = stator total inductance = $L_{ls} + L_m$
- L_r = rotor total inductance = $L_{lr} + L_m$

In equations (3.7) and (3.8) representing the generator dynamic, all variables are expressed with relation to the stator side. Flux linkage is the induction of an electromotive force through electromagnetic induction in one circuit due to a current variation in a different circuit. The relation between flux and currents is given by inductances. Self inductance is the ratio between flux in a winding and current in this same winding while mutual inductance is the relation between a winding's flux and the current in a different winding. The total equation is given by:

$$\begin{aligned} L_s &= L_{ss} - L_{sm} + L_{ls} \\ L_r &= L_{rr} - L_{sm} + L_{lr} \end{aligned} \tag{3.9}$$

It is standard practice to apply the Park transform to the system variables in equations (3.7) and (3.8) to remove the dependance between magnetic flux and rotor position. This operation also has the great advantage of setting 2 independent systems of variables - the d-axis and q-axis - that allows each converter to independently control two variables.

Figure 3.3 shows the two reference frames used to transform the stator and rotor variables. Appendix B shows the details of this transform. In this operation, the oscillating voltage and current signals are transformed in 2 constant signals to allow the development of 2 independent set of equations relating rotor and stator currents, voltages and fluxes. All variables can now be expressed along two axis (d and q), facilitating a great deal the design of the control algorithm. Using the reference frame shown on Figure 3.3, the d-axis variables will affect the reactive power while the q-axis variables will affect the active power.

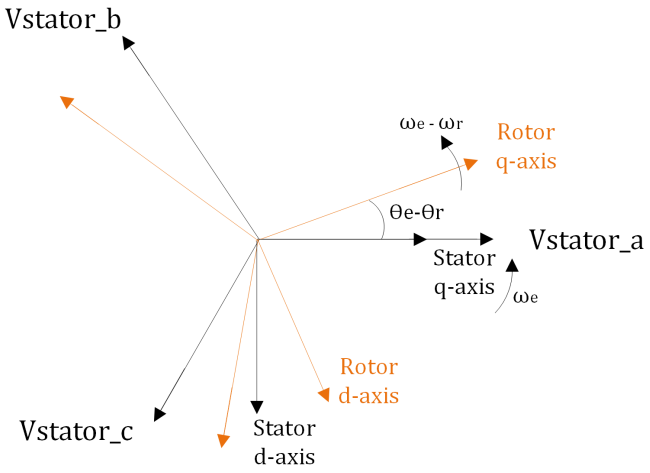

Figure 3.3: Reference frames used in Park transform

The grid angle θ_e and the rotor angle θ_r are required to compute the slip angle θ_{slip} and rotate the reference frame at the slip frequency ($\omega_{slip} =$

$\omega_e - \omega_r$). Once the 3-phase variables have been sent in the dq reference frame, the generator equations can be expressed with reference to the d and q frames:

$$\upsilon_{sd} = R_s i_{sd} + \frac{d\lambda_{sd}}{dt} - \omega_s \lambda_{sq} \tag{3.10}$$

$$\upsilon_{sq} = R_s i_{sq} + \frac{d\lambda_{sq}}{dt} - \omega_s \lambda_{sd} \tag{3.11}$$

$$\upsilon_{rd} = R_r i_{rd} + \frac{d\lambda_{rd}}{dt} - \omega_{slip} \lambda_{rq} \tag{3.12}$$

$$\upsilon_{rq} = R_r i_{rq} + \frac{d\lambda_{rq}}{dt} - \omega_{slip} \lambda_{rd} \tag{3.13}$$

While the new flux equations are the following:

$$\lambda_{rq} = L_s i_{rq} + L_m i_{sq} \tag{3.14}$$

$$\lambda_{rd} = L_r i_{rd} + L_m i_{sd} \tag{3.15}$$

$$\lambda_{sq} = L_s i_{sq} + L_m i_{rq} \tag{3.16}$$

$$\lambda_{sd} = L_s i_{sd} + L_m i_{rd} \tag{3.17}$$

Figure 3.4 [16] shows the relation between the generator variables in the d and q axes in a equivalent generator schematic:

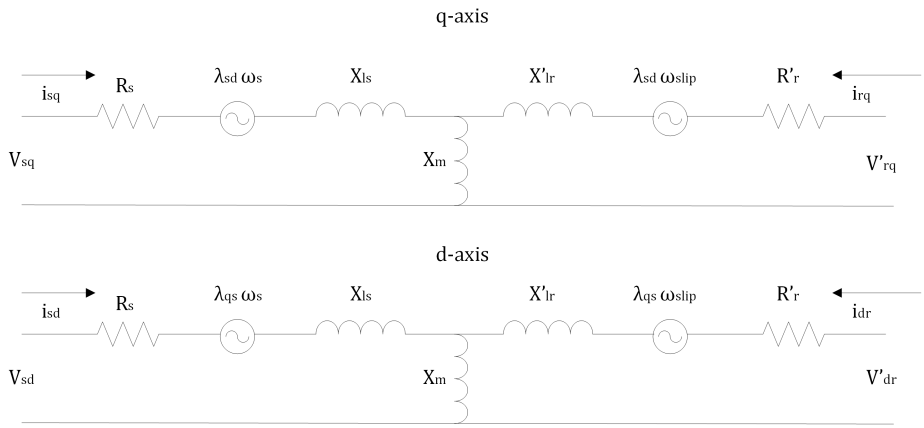

Figure 3.4: Schematic of generator governing equations along d and q axis

The overall system equations can also be re-written with relation to the rotating frames:

$$P_{tot} = P_{rot} + P_{stat} = \frac{3}{2}(v_{qr}^{'} i_{qr}^{'} + v_{dr}^{'} i_{dr}^{'} + v_{qs} i_{qs} + v_{ds} i_{ds}) \tag{3.18}$$

$$Q_{tot} = Q_{rot} + Q_{stat} = \frac{3}{2}(v_{qr}^{'} i_{dr}^{'} - v_{dr}^{'} i_{qr}^{'} + v_{qs} i_{ds} - v_{ds} i_{qs}) \tag{3.19}$$

3.4 Converter modeling

The B2B converter is made of two converters each able to act as an inverter and a rectifier, as required. The rotor side converter (RSC) and the grid side converter (GSC) are respectively connected to the rotor circuit and to the grid through impedances.

The electronic power converters used in the test bench each contain 6 IGBT switches. A detailed power electronic simulation in Matlab/Simulink of these switches would make the system more complex and increase considerably the simulation time. For this reason, it was left out of the simulation and the converter controller outputs are directly fed in the DFIG model. For simulation purposes, the electronic power converter is represented by three ideal voltage sources.

3.4.1 Connection of GSC to the grid

The connection between the GSC and the grid can however be modeled by the grid's filter impedance R_{grid} and L_{grid}.

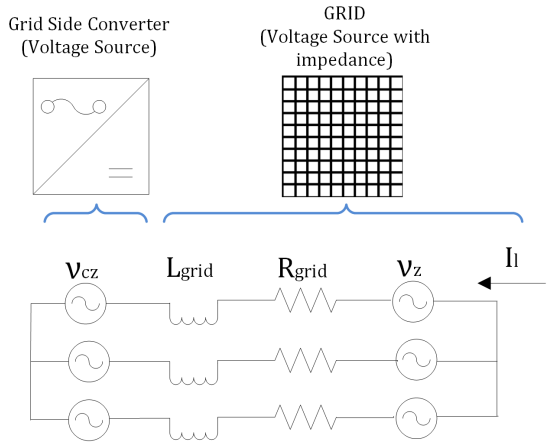

Figure 3.5: Connection of GSC to grid

The equation representing this connection is:

$$v_z - v_{cz} = R_{grid} i_l + L_{grid} \frac{di_l}{dt} \tag{3.20}$$

The control algorithm being developed along two separate axis (d and q), this equation can be expressed in the same way:

$$v_{zd} - v_{czd} = R_{grid} i_{ld} + L_{grid} \frac{d}{dt} i_{ld} - \omega_s L_{grid} i_{lq} \tag{3.21}$$

$$v_{zq} - v_{czq} = R_{grid} i_{lq} + L_{grid} \frac{d}{dt} i_{lq} - \omega_s L_{grid} i_{ld} \tag{3.22}$$

3.4.2 DC bus Model

The fast variation of active power flow occuring in the rotor circuit require the GSC to quickly adapt its output in order to keep the DC bus bar voltage (E_{DC}) constant. A power balance of the B2B converter is necessary in order to equalise input and output.

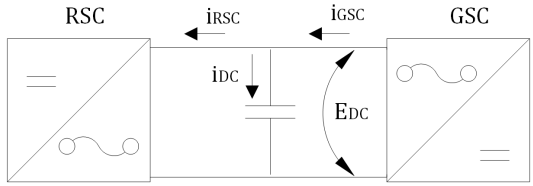

Figure 3.6: Energy balance of the B2B converter

Equation (3.23) relates the system power flows to E_{DC}. It is standard practice to include a DC chopper as a protection element in the DC bus bar. In case of an excedent increase of E_{DC} during grid voltage drop for example, the chopper is turned on and absorbs the excedent energy from the bus bar. This element is however not represented in the simulation since it is not installed on the test bench.

$$E_{DC} = CTE + \frac{1}{C_{DC}} \int_0^t i_{DC} \cdot dt = CTE + \frac{1}{C_{DC}} \int_0^t \left(\frac{P_{GSC} - P_{RSC}}{E_{DC}} \right) dt \tag{3.23}$$

Where:

- CTE is the initial DC bus voltage, corresponding to its reference value E^*_{DC}
- C_{DC} is the capacitance of the DC link capacitor

4 Converter control algorithm

Each converter in the DFIG rotor circuit has the ability to independently control 2 parameters. The rotor-side converter (RSC) controls the stator active power and reactive power (P_s and Q_s) while the grid-side converter (GSC) controls the rotor circuit reactive power and the DC bus bar voltage (Q_r and E_{DC}). This chapter is divided in 3 sections:

- The high level system: it determines the optimal electromagnetic torque corresponding to the machine speed to allow maximal power extraction in the design zone.
- The rotor-side control: two different orientation frames are compared: stator voltage oriented control (VOC) and flux oriented control (FOC). A sensorless approach used to obtain the rotor angle is also described.
- The grid-side control: reference current calculation and current control loop are presented.

Figure 4.1 shows the reference values entered in the B2B converter. Both reference reactive power Q_s and Q_r are usually set to zero and can be modified depending on the grid requirements. The DC link reference voltage is a fixed value while the reference torque is determined by the high level system.

4.1 High level system

The role of the high level system is to determine the torque at which the generator must operate to maintain operation at the equilibrium point on

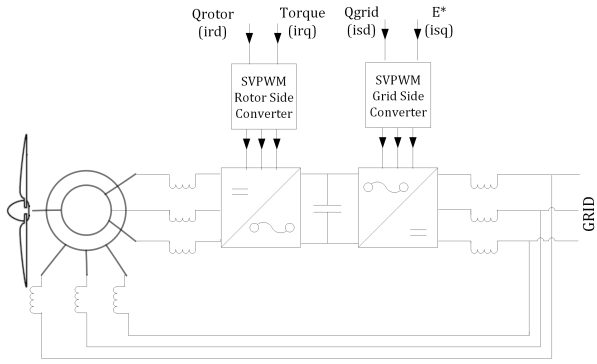

Figure 4.1: Reference values entered in B2B converter

the optimal torque curve. The first step towards this optimization is the derivation of equation (3.4) with relation to the tip speed ratio λ, which gives:

$$\lambda_{opt} = \frac{c_2 c_7}{c_2 c_7 c_9 + c_6 c_7 + c_2} \tag{4.1}$$

The optimal tip speed ratio is then substituted in the equation of the coefficient of power, leading to the following direct relation:

$$C_p^{opt} = \frac{c_1 c_2 \frac{-c_4 c_7 \beta^{c_5} + c_3 c_7 \beta + c_6 c_7 + c_2}{c_2}}{c_7} \tag{4.2}$$

The optimal coeffient of power can be used in equation (3.1), which, when simplified, gives:

$$\Gamma_{opt} = K_{CP} \cdot \omega_t^2 \tag{4.3}$$

The ability to vary the turbine speed allows adapting the tip speed ratio to the wind speed while operating in the design area in order to maintain C_p to its maximal value. Figure 4.2 show the mechanical torque resulting from different wind speeds in a 5.5 kW turbine and the optimal torque curve, which the RSC high level system intends to follow.

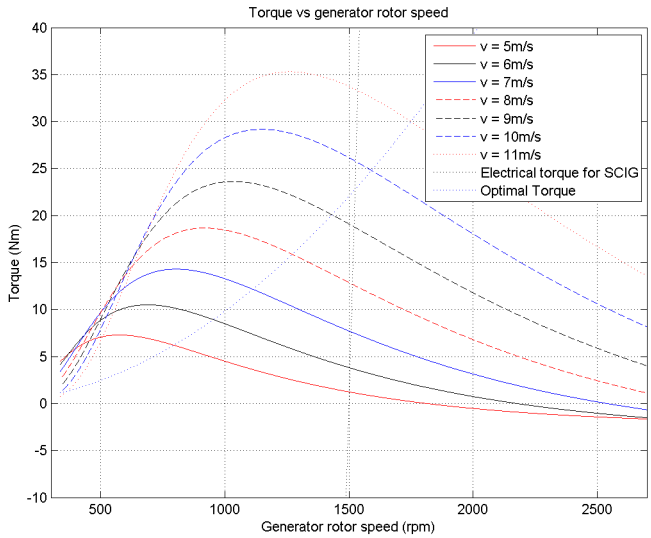

Figure 4.2: Mechanical torque at different wind speeds and optimal torque curve

As explained in section 2.1, the system can be operated in two modes: partial load and full load. When operating in the full-load mode, the high level system adjusts the blade orientation (pitch) in order to reduce the mechanical torque and keep the power to its rated value. It should be noted that, in the present report, the design of a pitch control was not the focus of work since it cannot be implementated on the test bench. Hence, in the above equations, the blade pitch angle is kept to $\beta = 0$, simplifying the equations considerably. Using the selected reference frame orientation, the quadrature-axis current i_q and the direct-axis current i_d respectively determine the value of the active power and the reactive power.

4.1.1 Effect of high level system on operating point

This section deals with the impact of the high level system strategy on the electrical torque curve. The turbine operating point is fixed by the equilibrium point between the mechanical and electrical torque. By controlling its output voltage, the RSC varies the equivalent impedance (Z_{eq}) of the rotor circuit, which in turn modifies the electrical torque curve to reach the optimal equilibirum point. This logic is explained in details in the present

section and its impact on the torque curve is shown in Figure 4.3. The generator data used for simulation is shown in appendix A.

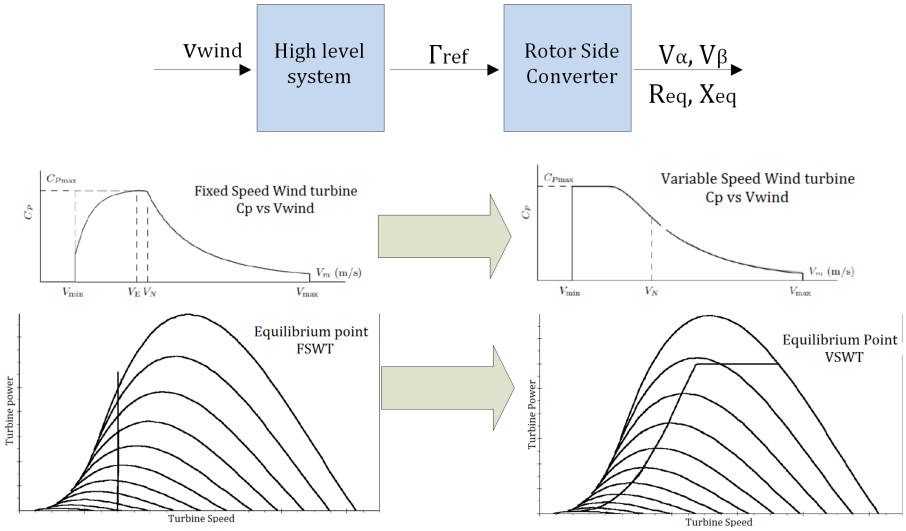

Figure 4.3: Effect of rotor circuit voltage control on operating point

The simplified equivalent circuit of a DFIG generator is shown on Figure 4.4. It differs from the standard equivalent circuit of a SCIG generator by the converter equivalent impedance (R_{eq} and X_{eq}), which can be controlled.

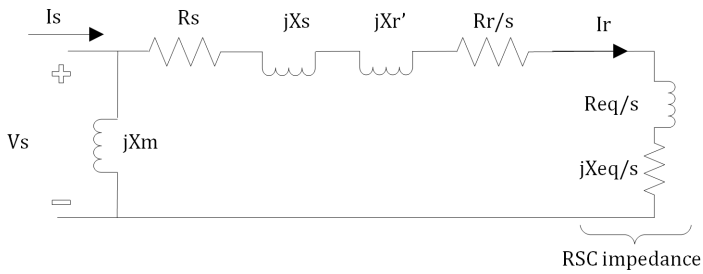

Figure 4.4: Simplified electrical circuit of a DFIG

The following equations describe the process leading to the optimal torque curve. First, in order to gather the whole system in the stator circuit, the converter impedance is divided by the slip:

$$Z_{eq} = R_{eq} + j\omega_{slip}L_{eq} \tag{4.4}$$

$$Z_{eq}/s = R_{eq}/s + j\omega_{slip}L_{eq}/s = R_{eq}/s + j\omega_s L_{eq} \tag{4.5}$$

The value of each optimal torque point (ω_{opt} and Γ_{opt}) is gathered from the high level system. Then, all generator variables are calculated:

$$I_s = \frac{V_s \pm \sqrt{V_s^2 - \frac{4R_s T_m \omega_s}{3P}}}{2R_s} \tag{4.6}$$

$$V_m = V_s - I_s(R_s + j\omega_s L_{ls}) \tag{4.7}$$

$$I_m = \frac{V_m}{j\omega_s L_m} \tag{4.8}$$

The rotor current and voltage are calculated:

$$I_r = I_s - I_m \tag{4.9}$$

$$V_r = sV_m - I_r(R_r + js\omega_s L_{lr}) \tag{4.10}$$

Finally, the equivalent impedance of the MSC is given by:

$$Z_{eq} = \frac{V_r}{I_r} \tag{4.11}$$

Figure 4.5 shows the variation of X_{eq} and L_{eq} through a range of slips. As shown, X_{eq} and R_{eq} are positive in supersynchronous mode and negative in subsynchronous mode. This occurs because of the change in current direction when the turbine speed crosses the synchronous speed.

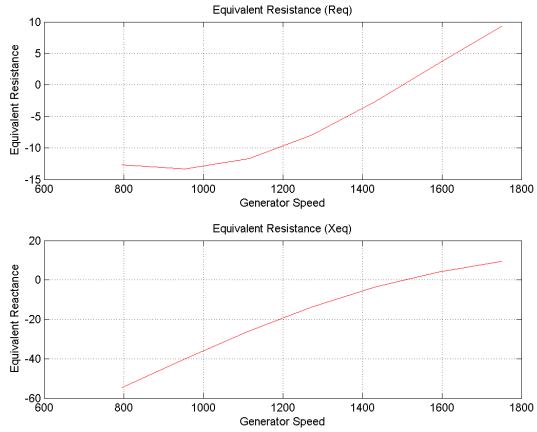

Figure 4.5: Effect of turbine speed variation on RSC equivalent resistance and reactance

Once the equivalent impedance is known, the standard electrical torque and power calculations are used to obtain the optimal curves shown on Figure 4.6. The DFIG subscript represents the values of rotor circuit impedance, power and electromagnetical torque once speed control is applied by the rotor side converter.

$$Z_{r_{DFIG}} = (\frac{R_r}{slip} + R_s + \frac{R_{eq}}{slip}) + j(X_{lr} + X_{ls} + \frac{X_{eq}}{slip}) \tag{4.12}$$

$$I_{r_{DFIG}} = \frac{V_s}{Z_r} \tag{4.13}$$

$$P_{DFIG} = 3 \mid I_r^2 \mid \frac{1 - slip}{slip}(R_r + R_{eq}) \tag{4.14}$$

$$\Gamma_{DFIG} = \frac{3V_s^2}{(R_s + R_r/slip + R_{eq}/slip)^2 + (X_{ls} + X_{lr} + X_{eq}/slip)^2} \frac{R_r + R_{eq}}{slip} \tag{4.15}$$

Figure 4.6 shows the effect of the impedance variation on the electrical torque. As seen that, when the wind speed increases from 9 m/s to 11 m/s, the rotational speed increases from 1431,8 to 1750 rpm by following the optimal torque curve. Two lines of the same color represent the mechanical torque and its corresponding electromagnetic torque. Their intersection

point is exactly on the optimal torque curve. The rated power is reached in the super-synchronous region at a slip of -0.1667 and a speed of 1750 rpm.

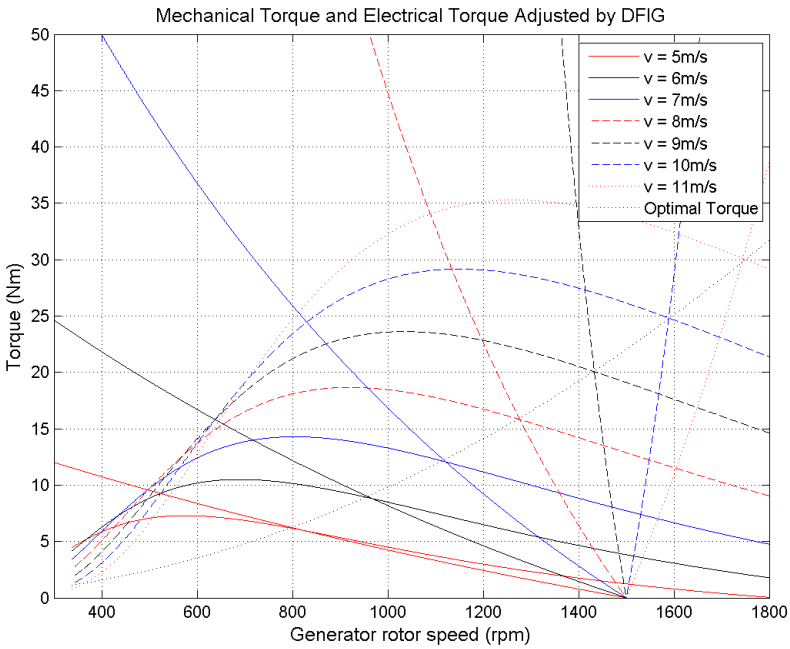

Figure 4.6: Effect of variation of rotor circuit impedance on electrical torque.

4.2 Rotor side control

The rotor-side converter receives measurements of rotor circuit variables and is responsible of managing the reactive power flow between the stator and the grid as well controlling the generator electrical torque. Its input variables are not aligned with the stator reference frame. However, it is precisely the stator output that must be controlled. In order for the RSC to compute an output consistent with the stator's variables, the rotor variables expressed in the rotor d-q reference frame must be rotated in order to be oriented with the control reference frame. In litterature, two different variables are used to perform this orientation: the stator voltage (V_s) and the stator flux (λ_s).

4.2.1 Control reference frame orientation

The rotor variables orientation must follow the orientation of the selected orientation parameter. In this report, two algorithms are implemented based on two different orientation parameters: stator voltage oriented control (VOC) and stator flux oriented control (FOC). Once the vector of this parameter is computed in the rotor reference frame, its relative angle (δ) to the rotor reference frame is calculated and the rotor variables are transformed into the new control-oriented frame. Figure 3.3 shows the position of the reference frames used in this report and the angles required to realize the Park transform.

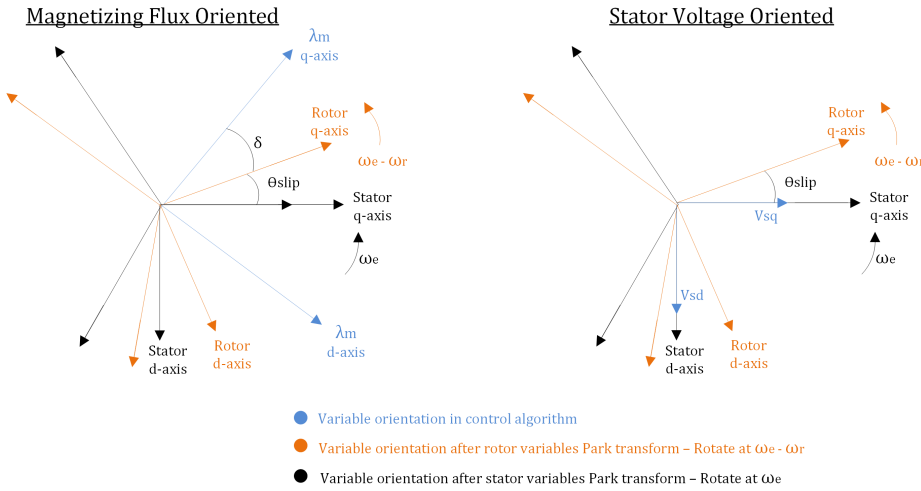

Figure 4.7: Reference frame orientation of flux-oriented and voltage-oriented control

The equations used in the orientation process are:

$$\begin{aligned} S_{rd} &= S'_{rq} sin(\delta) + S'_{rd} cos(\delta) \\ S_{rq} &= S'_{rq} cos(\delta) - S'_{rd} sin(\delta) \end{aligned} \tag{4.16}$$

Where:

- S' represents a d-q rotor variable expressed in the rotor reference frame rotating at slip frequency.

- S represents the same rotor variable oriented along the control reference frame.
- δ represents the alignment angle by which the rotor reference frame must be rotated.

4.2.2 Stator voltage oriented control (VOC)

In a DFIG system, it is relatively simple to implement the VOC since the stator is connected to the grid and its voltage can be considered constant. The stator voltage oriented equations can be implemented more easily since they do not require the computation of the stator flux. As shown on Figure 4.8, the variables required for RSC control are the stator quadrature voltage (V_{qs}), the stator frequency ω_e, the reference active power P_{ref} (or the reference torque Γ_{ref}) and the reactive power Q_{ref}.

Calculation of current reference values

The torque and reactive power equations valid for any q-d reference frame are [23]:

$$\Gamma_m = \frac{3P_pL_m}{2L_s}(-i_{qr}\lambda_{ds} + i_{dr}\lambda_{qs}) \tag{4.17}$$

$$Q_s = \frac{3}{2}(v_{sq}i_{sd} - v_{sd}i_{sq}) \tag{4.18}$$

The selected q-d reference frame shown in section 3.3 links the d-axis variables with the reference reactive power while the q-axis variables affect the reference torque. By replacing the values of i_{sq} and i_{sd} by their equivalence in terms of the stator flux and re-arranging equations (4.18) and (4.17), the reference currents equations are obtained.

$$i_{dr}^* = \frac{-2L_sQ^*}{3L_mv_{qs}} - \frac{v_{qs}}{\omega_sL_m} \tag{4.19}$$

The process leading to the equation of i_{qr} is described next. The stator flux approximated equations (4.20) are introduced in the torque equation (4.17) to obtain the complete torque equation (4.21)

$$\begin{aligned} \lambda_{ds} &= \frac{v_{qs} - R_si_{qs}}{\omega_s} \\ \lambda_{qs} &= -\frac{v_{ds} - R_si_{ds}}{\omega_s} \end{aligned} \tag{4.20}$$

$$\Gamma_m = \frac{3P_pL_m}{2\omega_sL_s}(-i_{qr}\upsilon_{qs} + R_si_{qs}i_{qr} + R_si_{ds}i_{dr} - i_{dr}\upsilon_{ds}) \tag{4.21}$$

From here, it is standard practice to neglect the stator resistance for simplification purposes. This assumption is valid for large WT but can lead to inaccuracies in the reference current calculation for small generators. This assumption is also done in the present simulation but the hypothesis should be confirmed during implementation on test bench given the relatively large value of R_s on small machines. The simplified reference current equation is:

$$i^*_{qr} = \frac{2\omega_sL_s\Gamma_m}{3P_pL_m\upsilon_{qs}} \tag{4.22}$$

4.2.3 Stator flux oriented control (FOC)

The flux oriented equations require more input variables since the stator flux must be computed as indicated in equations (3.16) and (3.17). The angle between the flux vector and the rotor reference frame is computed:

$$\begin{aligned} cos(\delta) &= \frac{\lambda_{sq}}{\sqrt{\lambda^2_{sq} + \lambda^2_{sd}}} \\ sin(\delta) &= \frac{\lambda_{sd}}{\sqrt{\lambda^2_{sq} + \lambda^2_{sd}}} \end{aligned} \tag{4.23}$$

Once all system variables $(i_{sd}, i_{sq}, \upsilon_{sd}, \upsilon_{sq}, i_{rd}, i_{rq})$ are rotated by this angle, the reference current values can be computed, keeping in mind that $\upsilon_{sd} = 0$:

$$i^*_{rq} = \frac{2L_s\Gamma_m}{3PpL_m\lambda_{sq}} \tag{4.24}$$

$$i^*_{rd} = \frac{-2L_sQ^*_s + L_m\upsilon_{sd}i_{rd} + \upsilon_{sd}\lambda_{sq}}{3L_m\upsilon_{sd}} = \frac{-2L_sQ^*_s}{3L_m\upsilon_{sq}} \tag{4.25}$$

The first expression in equation (4.25) can be used in the simulation while it is easier to use the second expression for implementation on a test bench. The difference is minimal since $\upsilon_d \approx 0$. Furthermore, as expected, the reference currents equations are very similar between FOC and VOC. The main difference is the stator variable being used: υ_s or λ_s.

Thus, one important difference between VOC and FOC is the number of inputs required to orientate the control variables and compute the reference current. Figure 4.8 shows the inputs required in each case.

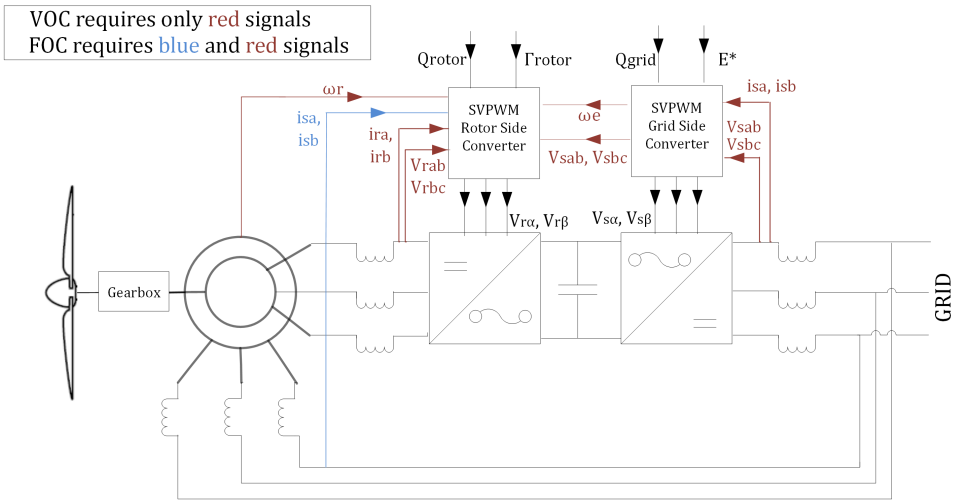

Figure 4.8: Input signals required for VOC and FOC

4.2.4 Control variables re-alignment

In the FOC algorithm, once the control variables have been calculated in the control reference frame (the blue reference frame on Figure 4.7), they must be re-aligned with the rotor reference frame. This is done in order to send to the PWM references values that are synchronous with the rotor variables (orange frame in Figure 4.7). The equations used in the re-alignment process calculate the inverse of equation 4.16:

$$\begin{aligned} S'_{rd} &= -S_{rq}sin(\delta) + S_{rd}cos(\delta) \\ S'_{rq} &= S'_{rq}cos(\delta) + S_{rd}sin(\delta) \end{aligned} \tag{4.26}$$

4.2.5 RSC current control loop

Once the current reference values have been computed, it is necessary to analyze the overall system dynamic to design properly the controller responsible for regulating the dynamic of the converter output voltage. The rotor circuit current control is done using a direct synthesis algorithm.

Decoupling terms

Before applying the current control function, the governing equations are expressed in two separate reference frames, avoiding cross-coupling. Indeed, equations (3.10) to (3.13) all include d-axis and q-axis terms. A simple technique is to re-introduce the undesirable terms after the PI control has been executed. The objective is to obtain a linear system to which the Laplace transform can be easily applied. Thus, if the current derivative is neglected, the resulting equations of the controlled portion of the voltage are:

$$\begin{aligned} \hat{v_{rd}} &= R_r i_{rd} + L_r \frac{d}{dt} i_{rd} \\ \hat{v_{rq}} &= R_r i_{rq} + L_r \frac{d}{dt} i_{rq} \end{aligned} \tag{4.27}$$

Current control loop

Figure 4.9 shows the role of the current control loop transfer function R(s) in the overall dynamic. In this case, the designer selects the overall dynamic M(s) as a first order system. The time constant of the overall function M(s) is called τ while the system dynamic G(s) representing the interconnection between the RSC and the rotor has a time constant of δ.

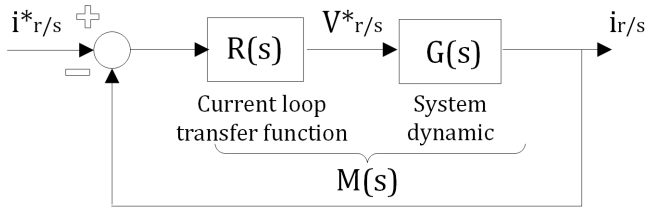

Figure 4.9: System transfer functions in current control

The overall dynamic includes the joint effect of G(s) and R(s):

$$M(s) = \frac{G(s)R(s)}{1 + G(s)R(s)} \tag{4.28}$$

Using equation (4.27), the 3-phase side of the RSC can be expressed as a first order system:

$$i_{r,dq} = \begin{vmatrix} \frac{1}{R_r + L_r s} & 0 \\ 0 & \frac{1}{R_r + L_r s} \end{vmatrix} \hat{v_{r,qd}} \tag{4.29}$$

Thus, the generator dynamic, in this case equivalent to the system dynamic, can be represented by the following equation:

$$G(s) = \frac{i_{lqd}}{\hat{v_{r,qd}}} = \frac{1}{R_l + L_l s} \tag{4.30}$$

Since the overall dynamic is the current relationship between real and reference value

$$M(s) = \frac{i_{qd}}{i^*_{qd}} = \frac{1}{1 + s\delta} \tag{4.31}$$

If M(s) and G(s) are first order transfer functions, by putting together equations (4.28) and 4.30, one gets:

$$R(s) = \frac{M(s)}{G(s)(1 - M(s))} = \frac{\tau}{K\delta} + \frac{1}{sK\delta} \tag{4.32}$$

Feedforward

The FOC control loop requires a feedforward loop, in which he elements that are not sent through the PI controller are added to the controlled part. This process is shown on Figure 4.11. In the case of voltage-oriented control, a feedforward loop is not required because of the assumption to neglect R_s in equation (4.21). This eliminated the cross-coupling terms and simplified the reference current equation, as shown on Figure 4.10.

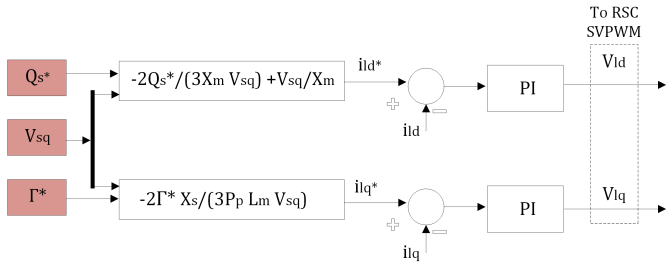

Figure 4.10: Complete control in voltage-oriented control

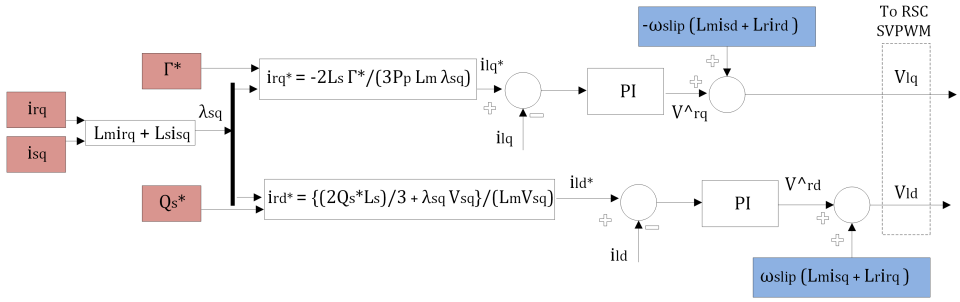

Figure 4.11: Complete control in flux-oriented control

4.3 Grid side control

By adjusting its output voltage, the grid-side converter controls the reactive power flow in the rotor circuit Q_r and keeps the DC bus voltage E_{DC} constant. Like in the RSC, two independant set of equations are put in place by the application of the Park transform.

4.3.1 DC link control loop

The DC bus voltage control is done through the q-axis current. Its design is more complex than the RSC controllers due to the interdependant control loops occuring simultaneously. As seen on Figure 4.12, the current reference is continuously calculated from the voltage error, i.e. the difference between the reference voltage and the measured one.

This controller is designed by first making two assumptions: the converter is ideal (losses are neglected) and the DC bus bar voltage dynamic is much slower than the internal current loop, given the large DC link capacitor. Considering a reference frame oriented such that $v_{ds} = 0$, a direct relationship is found between i_{qr} and i_{GSC} (see Figure 3.6):

$$E_{DC} \cdot i_{GSC} = \frac{3}{2}(V_{czq} i_{lq}) \tag{4.33}$$

From the balance of currents in the DC link given by equation (3.23), the integral term is included to compute the DC link voltage. As shown on Figure 4.12, the system transfer function for E_{DC} is based on the dynamic of two PI: C2(s) represents the controller bringing the voltage error to zero and G(s) is the system transfer function representing the bus bar dynamic.

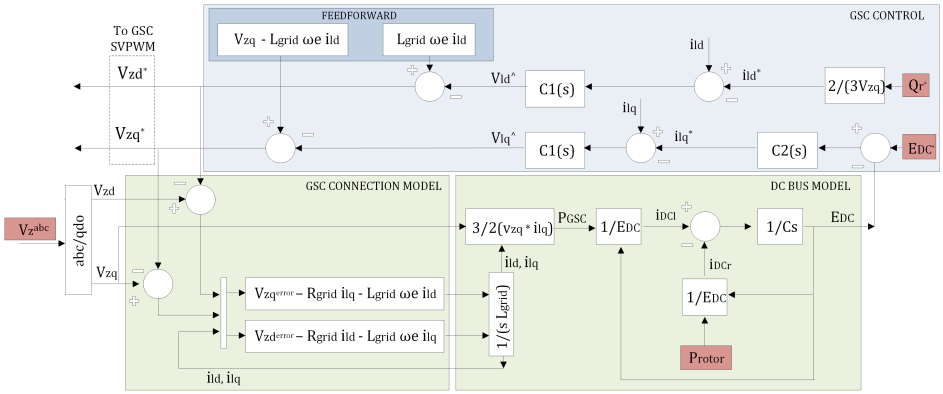

Figure 4.12: Control Schematic in GSC

As explained in [4], a direct method to obtain the controller parameters of C1(s) is to obtain the overall dynamic of C2(s) and G(s).

The transfer function C2(s) is set as a single order controller:

$$C2(s) = K_{p,DC} + \frac{1}{s} K_{i,DC} \tag{4.34}$$

So the overall function becomes:

$$\frac{E}{E^*} = \frac{C2(s)G(s)}{1 + C2(s)G(s)} = \frac{\frac{K_1 K_{p,DC}}{C} s + \frac{K_1 K_{i,DC}}{C}}{s^2 + \frac{K_1 K_{p,DC}}{C} s + \frac{K_1 K_{DC}}{C}} \tag{4.35}$$

On can recognize here a second order controller, so the parameters can be represented as:

$$K_{p,DC} = \frac{4C\omega_{DC}\xi_{DC}}{3K} \tag{4.36}$$

$$K_{i,DC} = \frac{2C\omega_{DC}^2}{3K} \tag{4.37}$$

4.3.2 Calculation of direct-axis current reference

The direct-axis reference current calculation is quite straight forward. It can be directly derived from equation (4.18):

$$i_{rd}* = \frac{2Q_r*}{3\upsilon_{rq}} \tag{4.38}$$

4.3.3 GSC current control loop

Decoupling

The connection between GSC and the grid reprsented by equations (3.21) and (3.22) is not a completely decoupled system i.e. variables in the d-axis and the q-axis are present in the same equation. A decoupling method must therefore be used in order to obtain a transfer function able to directly relate υ_{lq} to i_{lq} and υ_{ld} to i_{ld}. This relationship is similar to the one used to design the RSC current control loop in equation (4.30) but now represents the AC side of the GSC.

$$\begin{aligned}
\upsilon_{czd} &= -(\upsilon_{zd} + R_{grid}i_{ld} + L_{grid}\frac{d}{dt}i_{ld}) + \omega_e L_{grid}i_{lq} = \hat{\upsilon_{czd}} + \upsilon_{d,Decoupling} \\
\upsilon_{czq} &= -(\upsilon_{zq} + R_{grid}i_{lq} + L_{grid}\frac{d}{dt}i_{lq}) + \omega_e L_{grid}i_{ld} = \hat{\upsilon_{czq}} + \upsilon_{q,Decoupling}
\end{aligned} \tag{4.39}$$

The method of controller design is also direct synthesis. It considers the transfer function of the whole system M(s) and the dynamic G(s) of the connection to the grid in order to determine the current control transfer function R(s). This function will theorically lead to a system behaving as predicted by function M(s). However, some adjustments are usually necessary since there may be dicrepancies between the plant modeling G(s) and the real machine.

The systems transfer function can be derived by applying the Laplace transform to the previous equation:

$$i_{l,dq} = \begin{vmatrix} \frac{1}{R_{grid}+sL_{grid}} & 0 \\ 0 & \frac{1}{R_{grid}+sL_{grid}} \end{vmatrix} \upsilon^{\wedge}_{cz,dq} \tag{4.40}$$

Once again, by refering to Figure 4.9, if the function R(s) is represented by a first order PI controller, its control parameters are:

$$K_{pzq} = \frac{L_{grid}}{\delta} \tag{4.41}$$

$$K_{izq} = \frac{R_{grid}}{\delta} \tag{4.42}$$

Hence, the design of the transfer function linking the reference current (i^*_{qd}) to controlled voltage ($\hat{\upsilon_{cz}}$) takes in consideration the real dynamic linking voltage and current.

4.4 Sensorless control

The control approaches explained above require the rotor position to be known at every point in time. For this purpose, two solutions can be used:

1. The rotor position is measured continuously by an encoder and the signal sent to the rotor-side converter.

2. The rotor position is determined from the rotor and stator currents and voltages. This approach is known as the sensorless approach.

The use of an encoder represents an extra expense and the signal transmission can be problematic. The sensorless approach has been implemented extensively in the litterature: the methods used in [8], [14],[19], [20] and [24] show some advantages over the methods requiring rotor angle measurement:

- Simplicity of installation and reduced space use.

- Lower cost: in small to medium size machines, the sensor cost is considerable.

- Lack of reliability: an encoder is sensitive to external perturbations such as electromagnetic interferences.

However, a sensorless system can lead to its share of complications. The algorithm must be stable at a wide range of operating speeds and should not require the knowledge of any initial condition. Also, the flux equations being dependant of generator parameters, a variation of winding temperature can lead to a change in rotor and stator inductance and inacurracies between the calculated rotor speed and the actual one. Some of the methods used for rotor slip position are described below.

4.4.1 Current comparison method

In this algorithm described in reference [20], the slip estimation bases itself on the comparison between the estimated and measured rotor current. The rotor current is estimated from the active and reactive power transfered through the airgap. First, the electromotive force is determined from stator variables.

$$\begin{aligned} EMF_{\alpha s} &= \frac{1}{\omega_s}\frac{\psi_{\alpha s}}{dt} = \upsilon_{\alpha s} - r_s i_{\alpha s} \\ EMF_{\beta s} &= \frac{1}{\omega_s}\frac{\psi_{\beta s}}{dt} = \upsilon_{\beta s} - r_s i_{\beta s} \end{aligned} \tag{4.43}$$

The airgap power is then calculated:

$$\begin{aligned} P_{gap} &= i_s EMF_s = EMF_\alpha i_\alpha + EMF_\beta i_\beta \\ Q_{gap} &= i_s EMF_s - Q_m = EMF_\beta i_\alpha - EMF_\alpha i_\beta - Q_m \end{aligned} \tag{4.44}$$

Where Q_m is the reactive power present when no load is applied. Finally, the rotor current can be estimated from:

$$\begin{aligned} i_{qr}^{\wedge} &= -\frac{P_{gap}}{|EMF_s|} \\ i_{dr}^{\wedge} &= -\frac{Q_{gap}}{|EMF_s|} \end{aligned} \tag{4.45}$$

In litterature, this algorithm has shown good results despite its dependance on the stator self-inductance. Its main advantage is the fact that an estimation of the stator flux is not required.

4.4.2 Phase locking to d-q frame

This algorithm, explained in reference [21], uses a phase locked loop (PLL) and a voltage controlled oscillator (VCO) to track the rotor speed and finally align the rotor variables to the stator voltage.

Through a method similar to the one explained above, the difference between the measured and estimated stator voltage is entered in a VCO. Its output signal ocillates at a frequency that becomes locked with the rotor frequency ω_{rotor}. The feedback directly ensure that $\upsilon_{sd} = 0$, leading to a

voltage oriented control.

As with many sensorless methods, the disadvantage of this method is its dependance on generator parameters such as rotor, stator and magnetizing inductances during the stator voltage estimation (see equations (3.10) and (3.11)). The variation of inductance with the generator load and with time leads to substantial errors in the voltage estimation and in turn, in the rotor angle calculation.

4.4.3 Selected sensorless method

The sensorless algorithm that was used for simulation in this work is based on reference [24]. It can be separated in two blocks:

- The first block uses phase locked loops to calculate the rotor position and generates constant values of the rotor current in the rotor reference frame rotating at slip frequency.
- The second block aligns the rotor current with the stator voltage and applies RSC control to obtain the output voltage.

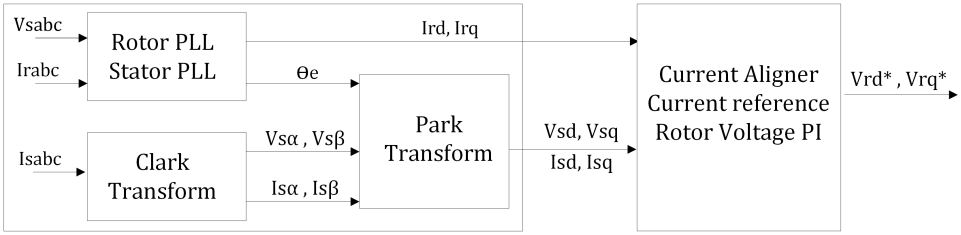

Figure 4.13: General schematic of sensorless algorithm

Stator voltage angle

The stator voltage angle is determined through a PLL and a VCO as shown on Figure 4.14.

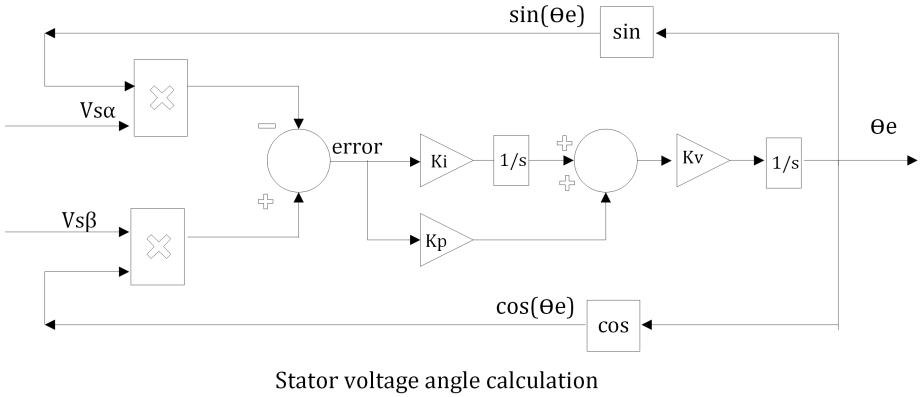

Figure 4.14: Block Diagram of Stator Angle Calculation

First, the Clark transform is applied to the measured voltage values.

$$\begin{bmatrix} V_\alpha \\ V_\beta \\ V_0 \end{bmatrix} = \frac{2}{3} \begin{bmatrix} 1 & -\frac{1}{2} & -\frac{1}{2} \\ 0 & \frac{\sqrt{3}}{2} & -\frac{\sqrt{3}}{2} \\ \frac{1}{2} & \frac{1}{2} & \frac{1}{2} \end{bmatrix} \begin{bmatrix} Vsin(\theta_e) \\ Vsin(\theta_e - \frac{2\pi}{3}) \\ Vsin(\theta_e + \frac{2\pi}{3}) \end{bmatrix} = \begin{bmatrix} Vsin(\theta_e) \\ Vcos(\theta_e) \\ 0 \end{bmatrix} \tag{4.46}$$

The error entered in the PI controller has the following form:

$$\begin{aligned} \varepsilon &= V_\alpha cos\hat{\theta} - V_\beta sin\hat{\theta} \\ &= Vsin\theta cos\hat{\theta} - Vcos\theta sin\hat{\theta} \\ &= Vsin(\theta - \hat{\theta}) \end{aligned} \tag{4.47}$$

For small values of θ, when the PLL output is synchronous with the input frequency, the error becomes:

$$\varepsilon \approx V(\theta - \hat{\theta}) \tag{4.48}$$

The PI controller parameters must allow for a fast phase locking and a small sensitivity to high frequency noise.

Rotor position angle

The rotor position angle (θ_r) is determined through a more complex system, as shown on Figure 4.15. It is similar to the system described above and takes in consideration the equation of slip frequency:

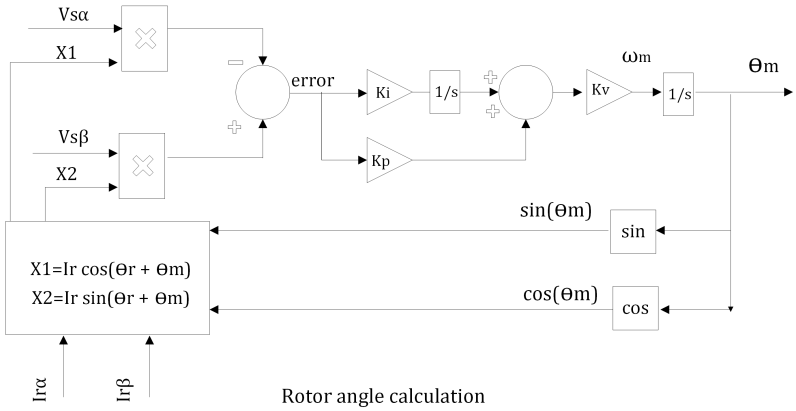

Figure 4.15: Block Diagram of Rotor Angle Calculation

$$\omega_{sync} = \omega_{rotor} + \omega_{slip} \tag{4.49}$$

This equivalence is used in the phase generator to compute the sinus and cosinus of the stator angle from the values of the mechanical and slip angles. It also requires the following trigonometric identity:

$$\begin{aligned} cos(X+Y) &= cosXcosY - sinXsinY \\ sin(X+Y) &= sinXcosY + cosXsinY \end{aligned} \tag{4.50}$$

Where $X = \theta_r$ and $Y = \theta_{rotor}$. The error used as the PI input is:

$$\varepsilon = V_\alpha I_r cos(\theta_r + \theta_m) - V_\beta I_r sin(\theta_r + \theta_m) \tag{4.51}$$

Which can be simplified as:

$$\begin{aligned} \varepsilon &= V_s I_r sin(\theta_s) cos(\theta_r + \theta_m) - V_s I_r cos(\theta_s) sin(\theta_r + \theta_m) \\ \varepsilon &= V_s I_r sin(\theta_s - (\theta_r + \theta_m)) \end{aligned} \tag{4.52}$$

Since the Clark transform of stator voltage gives:

$$\begin{bmatrix} V_{\alpha s} \\ V_{\beta s} \end{bmatrix} = \begin{bmatrix} V_s sin(\theta_s) \\ V_s cos(\theta_s) \end{bmatrix} \tag{4.53}$$

Hence, when the output of the VCO reaches the rotor frequency, the error becomes zero and the output is synchronous with the rotor frequency. The

mechanical angle is then used in the Park transform of the rotor variables, as it was done in the solutions using a position encoder.

Rotor current alignment

The constant values of the rotor current expressed along the rotor reference frame are aligned with the control reference frame, as described in Figure 4.16. The method results in a voltage-oriented system by keeping the value of V_{ds} to 0. This is performed by a PI whose output is the angle difference δ between the rotor and the stator reference frame. This angle is used to orientate the rotor currents, as shown in equation 4.16.

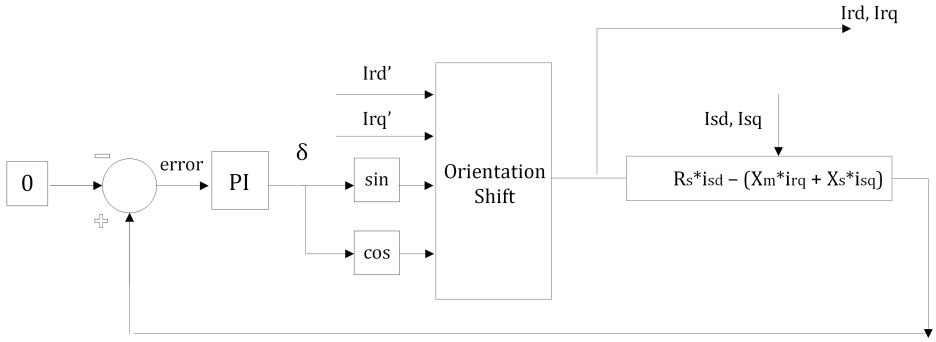

Figure 4.16: Block Diagram of Sensorless Alignment Algorithm

4.5 Control parameter tuning

This section presents the tuning of the control parameters based on the procedures presented in sections 4.2, 4.3 and 4.4.

4.5.1 Current control and DC link voltage control parameters

The control algorithms detailed above describe the calculation process for the the control parameters (K_p and K_i) of the different control loops. These parameters depend on the time constant (δ) of the system dynamic. In practice, this value must be selected to ensure that the overall dynamic is slower than the converter switching frequency. For both the RSC and GSC, a value

of $\delta = 30 \cdot T_{switch}$ has been selected. Using the RSC and the GSC switching frequencies of 12kHz and 24kHz respectively, the system is simulated using the control parameters shown in Table 4.2.

In the the DC link voltage control, the selection of the response frequency and damping ratio shown in equation (4.36) have an important effect on the response shape. Different values have been tried empirically and the optimal response occured with $\omega_{DC} = 10$ rad/s and $\xi_{DC} = 0.98$, as shown in table 4.1. A higher frequency resulted in higher peak and faster response.

ω_{DC} (rad/s)	$Capacitance$ (μF)	ξ	k	$K_{p,DC}$	$K_{i,DC}$
20	0.005	0.98	0.866	0.0754	0.3849

Table 4.1: DC Bus Voltage Control Parameters

RSC (current)		GSC (current)		GSC (DC voltage)	
K_p	K_i	K_p	K_i	K_p	K_i
2.152	300.698	11.561	753.98	0.0754	0.849

Table 4.2: Controllers parameters adapted to test bench equipment

4.5.2 Sensorless algorithm stability

The results of the sensorless approach are sensitive to the selection of the PI control parameters. In total, the RSC control includes five different PI controllers, as listed in table 4.3.

#	PI name	Input	Output
1	Rotor variables PLL	phase error	ω_{slip}
2	Rotor position VCO	phase error	ω_m
3	Stator voltage PLL	phase error	ω_e
4	Aligner	$V_{ds}^{\wedge}$	δ
5	Current loop	$i_{rdq}^{\wedge}$	$V_{rdq}*$

Table 4.3: PI controllers in sensorless algorithm

The dynamic created by the combination of all these PI requires to evaluate their role and size them accordingly. Next, the control parameters of the

PI controllers (1) and (2) are designed based on Figure 4.15. The voltage-controlled oscillator (VCO) receives the estimated speed and outputs the rotor angle:

$$T_{VCO} = \frac{\theta_m}{\omega_m} \tag{4.54}$$

While the PI computes the mechanical speed from the phase error:

$$T_{PLL} = \frac{\hat{\omega}}{\varepsilon} \tag{4.55}$$

Thus, when the VCO and the PLL transfer functions are joined and the error equation (4.52) is considered, the total transfer function of the rotor angle calculation is:

$$T_{total} = \frac{\hat{\omega}}{\omega} = \frac{V_s I_r (sK_p + K_i)}{s^2 + sV_s I_r K_p + V_s I_r K_i} \tag{4.56}$$

It becomes clear that the design of the total transfer function depends on system parameter and control parameters. In simulation, the rotor current varies between 0 and 6 A and the grid voltage is 690 V. Different values of K_p and K_i were used to test the transfer function response with a rotor current of $I_r = 4$ Amps. The following tables gathers values obtained from the Bode plots of the transfer function T_{total}.

As seen, it is hard to obtain a amplitude reduction greater than -5 dB at 4kHz with acceptable values of time delay. However, by using a higher value of the VCO gain (K_v) for both PLLs, it is found empirically that the whole system behaves in a much more stable way: the angle computation, the generator speed and the voltage and currents all show more stable response. The Bode plot of the total transfer function using these new control parameters is shown in Figure 4.17. For different values of I_r, the time delay at 100Hz ranges from -0.05 to -0.2 degrees while the amplitude at 4kHz ranges from -0.01 to 0.1 dB.The non-zero time delay between an input variation and the sensorless response could potentially be an issue with high frequency input. However, since grid voltage and wind speed variation are typically slower than the generator internal dynamic, the slight decrease in respond speed will not be an issue.

The method used in the previous steps to design the control parameters of PI controllers (1) and (2) is applied to design controller (3). Also, it is found empirically that controller (4) must have very small gain to remain stable. Finally, the design of controller (5) (the current controller) is described in

Kp	Ki	dB at 4kHz	Delay at 100 Hz
1		-5	−2.0
2		-1.8	−1.2
3	10	-0.9	−0.8
4		-0.5	−0.6
5		-0.4	−0.5
1		-5	−1.8
2	50 or	-2.0	−1.1
3	100	-1.0	−0.7
4		-1.0	−0.5
5		-0.9	−0.4
5		-0.25	−0.3
10		-0.07	−0.22
15	100	-0.04	−0.14
20		-0.02	−0.11
25		-0.01	−0.1
5		-0.3	−0.22
10	250 or	-0.07	−0.17
15	500	-0.04	−0.13
20		-0.02	−0.09
25		-0.01	−0.05

Table 4.4: Magnitude reduction and phase delay of transfer function

section 4.2.5. The control parameters used for simulation are listed in table 4.5.

#	PI name	Kp	Ki	Kv
1	Rotor angle: PLL θ_r	20	100	10
2	Rotor angle: VCO θ_r	10	40	10
3	V_s angle: PLL θ_e	20	100	-
4	Orientation: Aligner	0.001	0.005	-
5	Current loop	2	300	-

Table 4.5: Sensorless control parameters used for simulation

Figure 4.18 shows the real rotor angle and its calculated value. The accuracy of this calculation strongly depends on the correct selection of the PLL parameters. As seen, the error is kept to zero during a long period of time.

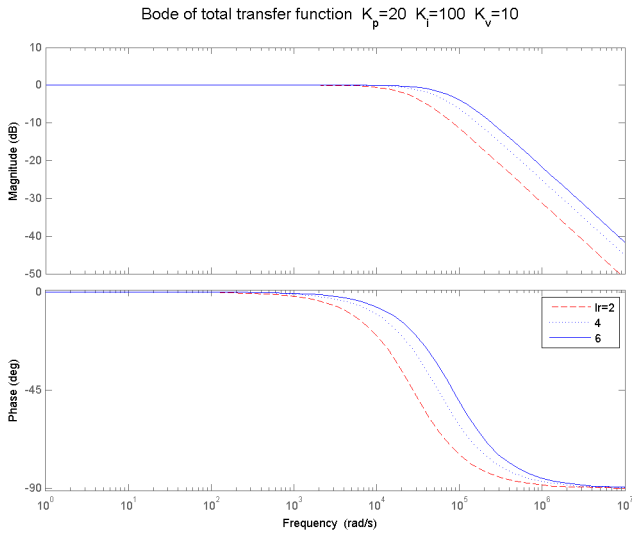

Figure 4.17: Bode of total transfer function

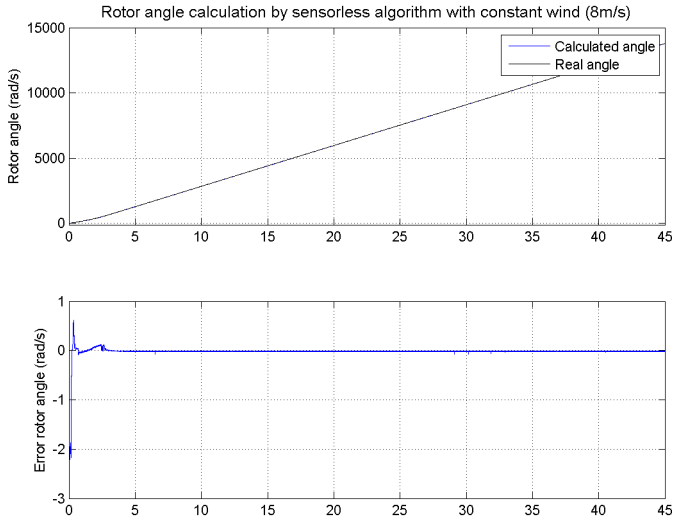

Figure 4.18: Rotor angle and error with constant wind speed

In real wind turbine operation, oscillations of the mechanical torque occur. Figure 4.19 shows the generator speed and rotor angle error response when a torque oscillation with a frequency of 5Hz and an amplitude of 2.5% occurs. As expected, the speed oscillates with a small amplitude while the angle error remains near zero.

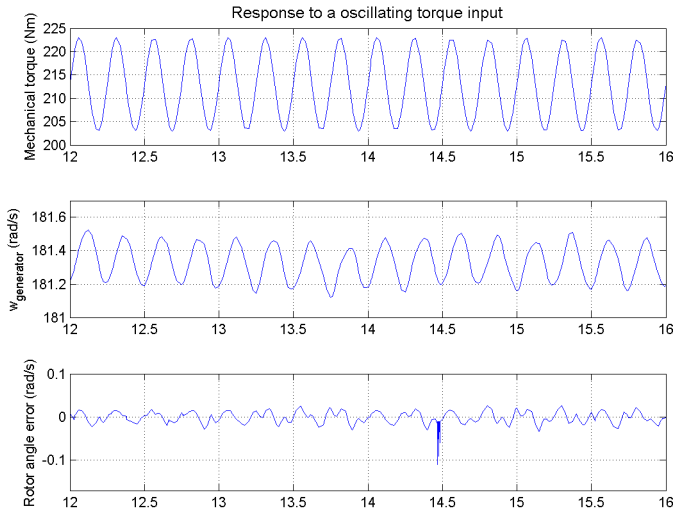

Figure 4.19: Rotor angle and speed response to oscillating mechanical torque

4.6 Simulation results

Before implementing the control algorithms on an experimental setup, the behavior of the complete system following different input changes is analyzed. Three cases are simulated: a wind speed increase and decrease (1), a grid voltage drop (2) and a step input of reference reactive power (3). The results obtained with voltage-oriented control, flux-oriented control and the sensorless approach are presented.

4.6.1 Wind speed ramp input

For simulation, it is considered that a realistic wind speed profile should not include step increase or decrease. Although sudden wind variation are

frequent due to high temporal variation of wind, these changes are not immediate since the speed is related to the wind kinetic energy. Hence, in the present simulation, the wind speed starts at 8 m/s, undergoes an increases of one second until it reaches 11 m/, remains there during three seconds and returns to its initial value during a one second decrease.

The first simulated case analyses the response to a wind speed ramp input and the results are shown on Figures 4.20 and 4.21. Since wind speed fluctuations first affect the high inertia turbine rotor, the response dynamic is slower that during variation of electrical variables. Thus, the speed, torque and power curves follow accurately and progressively the reference value. The active power response is exactly the same for both control approaches. The total reactive power varies slightly during a wind speed step input but is rapidly returned to its reference value.

Figure 4.22 shows the variation of speed and torque during a wind ramp input with a sensorless control. The reactive power curve is relatively noisy due to the complex controller dynamic described above. However, the speed, torque and active power all feature stable responses.

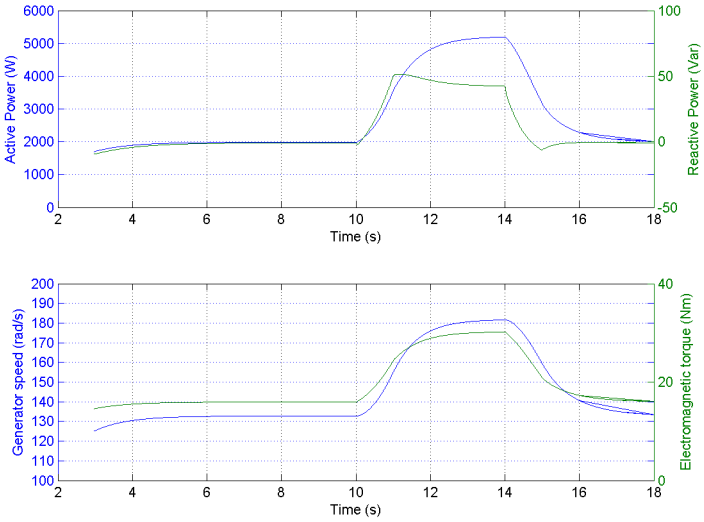

Figure 4.20: Response to wind speed ramp input in VOC (8-11-8 m/s)

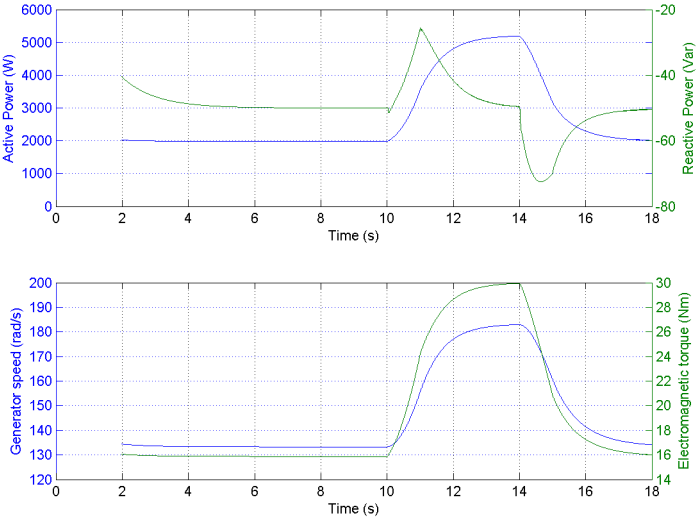

Figure 4.21: Response to wind speed ramp input in FOC (8-11-8 m/s)

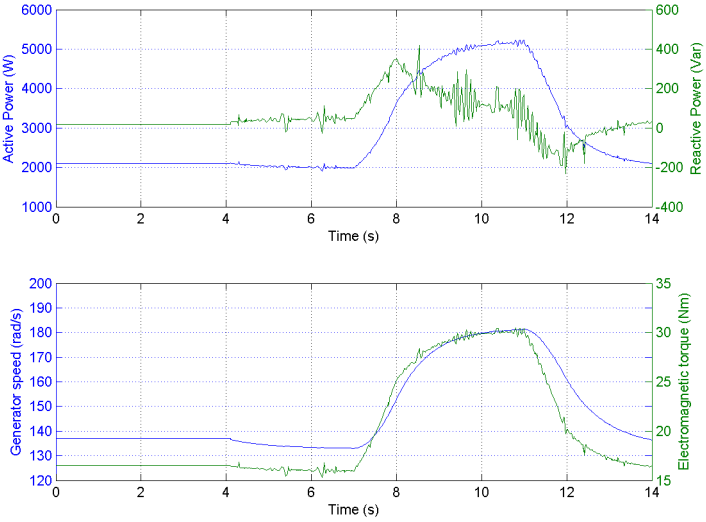

Figure 4.22: Response to wind speed ramp input in sensorless (8-11-8 m/s)

4.6.2 Grid voltage drop

A typical grid voltage drops is introduced in the system. Its duration is 150 μs, its intensity is 80 % and it occurs once the system has reached stable steady-state operation. The response is shown on Figures 4.23, 4.24 and 4.25. With VOC and FOC control as well as with the sensorless approach, the generator speed initially undergoes a small and short decrease and then rises until full grid voltage is recuperated, moment at which it gradually returns to its initial value. The first very short speed decrease is due to the sudden current peaks that create a small electrical torque peak. This electrical torque quickly increases to a value higher than the mechanical torque, which slows down the machine.The subsequent acceleration is due to the fact that all the electrical power cannot be injected to the grid and is momentarily stored in the form of kinetic energy.

For its part, the total active power is momentarily reduced since the low grid voltage prevents the machine from sending all its power to the grid. The reactive power undergoes sharp changes at the beginning and the end of the voltage sag, but finally returns to its design value. Given the absence of a pitch control, the turbine speed should be kept under its nominal value of 11 m/s. For this reason, the simulation was performed with $v_{wind} = 9m/s$. Finally, it is necessary to limit the output of both controllers through saturation tools. Indeed, the sharp change in grid voltage creates important transient current peaks whose amplitude must be limited to their nominal values.

As seen, the sensorless algorithm does not ensure system stability during a voltage drop. The sudden energy excess that cannot be sent to the grid creates important torque and active power oscillation. The use of sub-systems such as a DC chopper could lead to a more stable reaction to a grid voltage drop by evacuating this surplus of energy. It is also important to note that the complex controller dynamic occuring in the selected sensorless algorithm is not necessarily present in other sensorless methods using flux estimation techniques. The response of these methods is likely to be more stable during input variation.

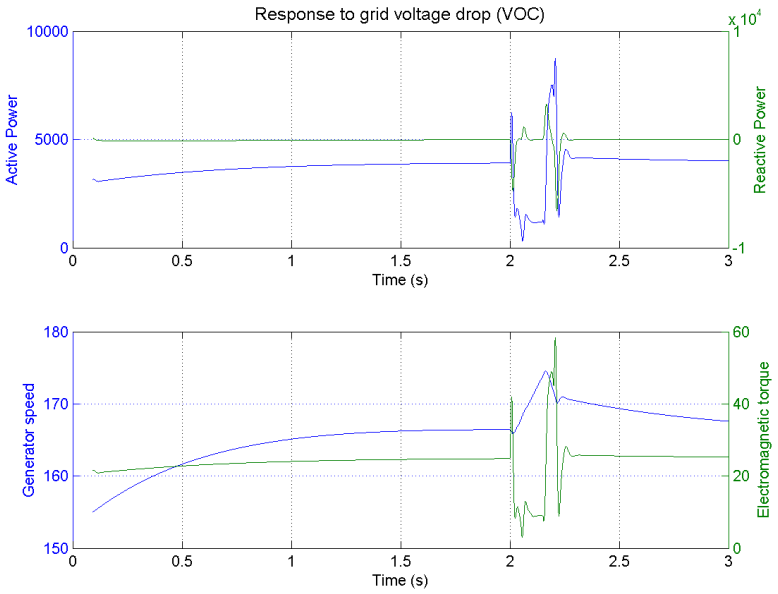

Figure 4.23: Response to grid voltage drop in VOC

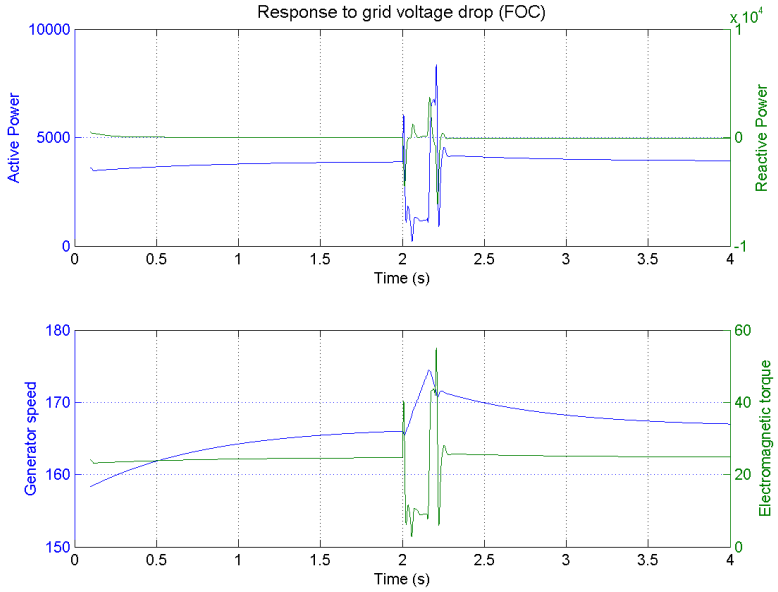

Figure 4.24: Response to grid voltage drop in FOC

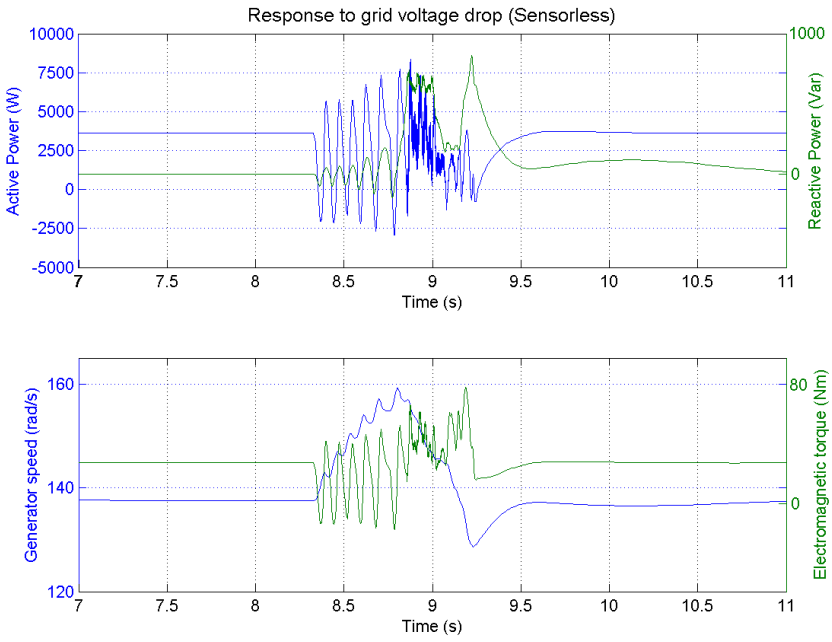

Figure 4.25: Response to grid voltage drop with sensorless algorithm

4.6.3 Reactive power step input

Here, the rotor circuit reference reactive power (Q_r^*) is suddenly increased to 500 Var and brought back to zero. This is directly followed by a step input of the stator circuit reference reactive power (Q_s^*). Step inputs are used since the wind turbine can be required to offer voltage support to the grid with very short notice. As seen, the effect on the active power (P_{rot} and P_{tot}) are short and of minimal intensity. The total reactive power Q_{tot} is the sum of the stator reactive power Q_s and the rotor reactive power Q_r. It follows exactly the reference value and shows small overshoots at the time of step input. In the sensorless case, the rotor circuit reactive power shows a stable response since it is controlled by the GSC. However, variables controlled by the RSC show more oscillation. Once again, this can be attributed to the dynamic occuring between the different controllers used in the sensorless algorithm

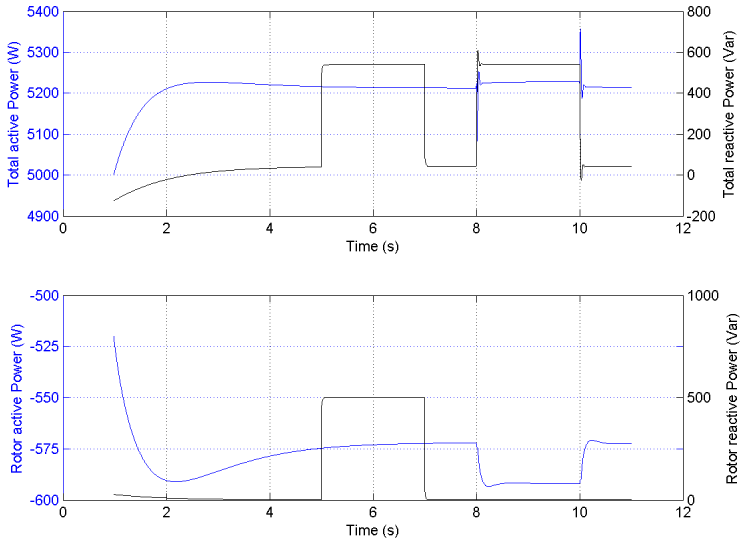

Figure 4.26: Power response to step input of Q_r^* and Q_s^* (VOC)

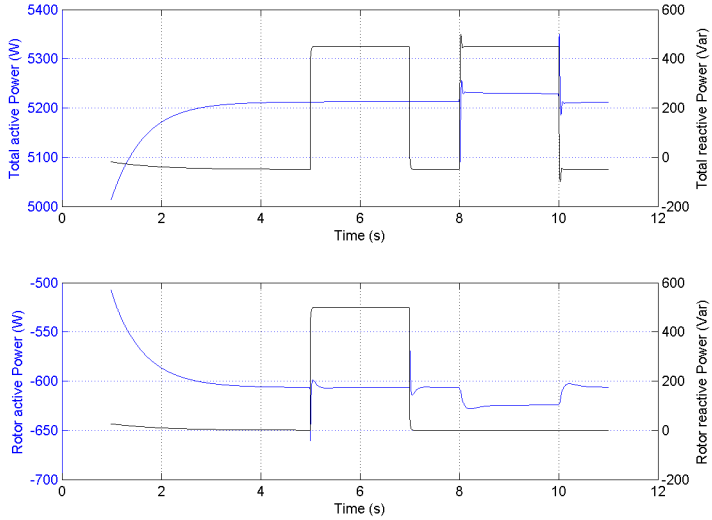

Figure 4.27: Power response to step input of Q_r^* and Q_s^* (FOC)

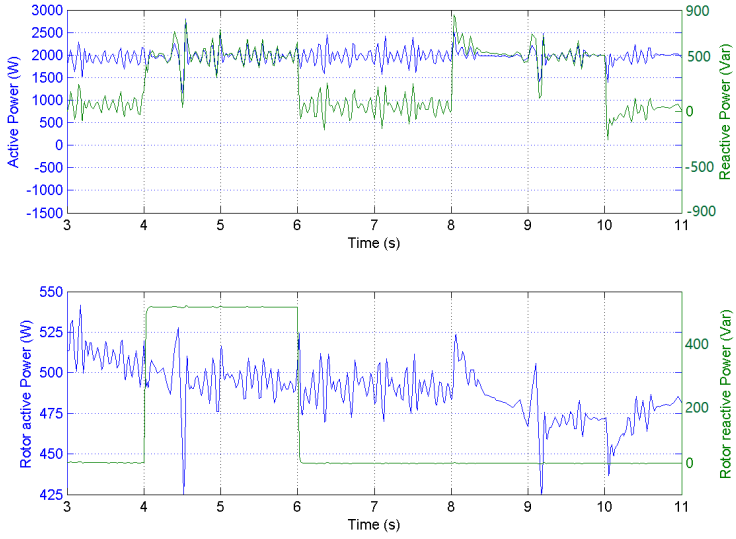

Figure 4.28: Power response to step input of Q_r^* and Q_s^* (Sensorless)

5 Test Bench

This section presents the implementation of the control algorithms on a wind turbine test bench. A 5.5 kW SCIG generator with 2 pole pairs and Y-Y connected was used in the set-up. The generator electrical parameters are shown in Appendix A. The layout of the test bench rotating components is shown on Figure 5.1.

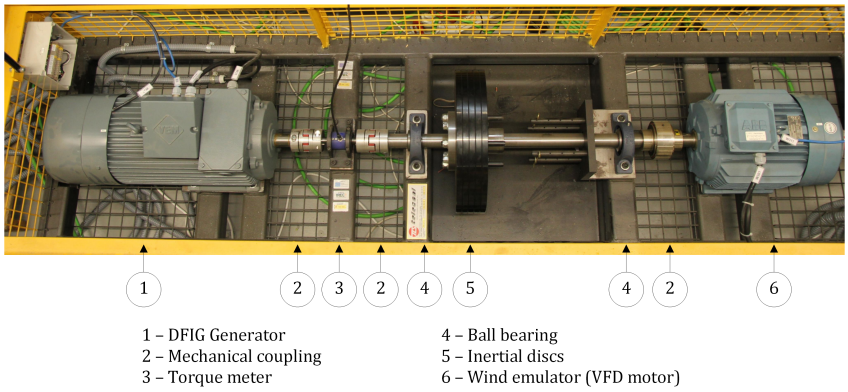

Figure 5.1: Rotating parts of test bench

Figure 5.2 shows the test bench interconnection and the available measurements while Figure 5.3 shows the back-to-back converter. The C^{++} code compiled by the CodeComposer (CCS) software is loaded on the RAM of each DSP through a J-TAG emulator. During testing, two separate variable

transformers are used to connect the stator and the GSC to the grid. This solution facilitates the start-up process by allowing to control the induced rotor currents but is not used in real implementation.

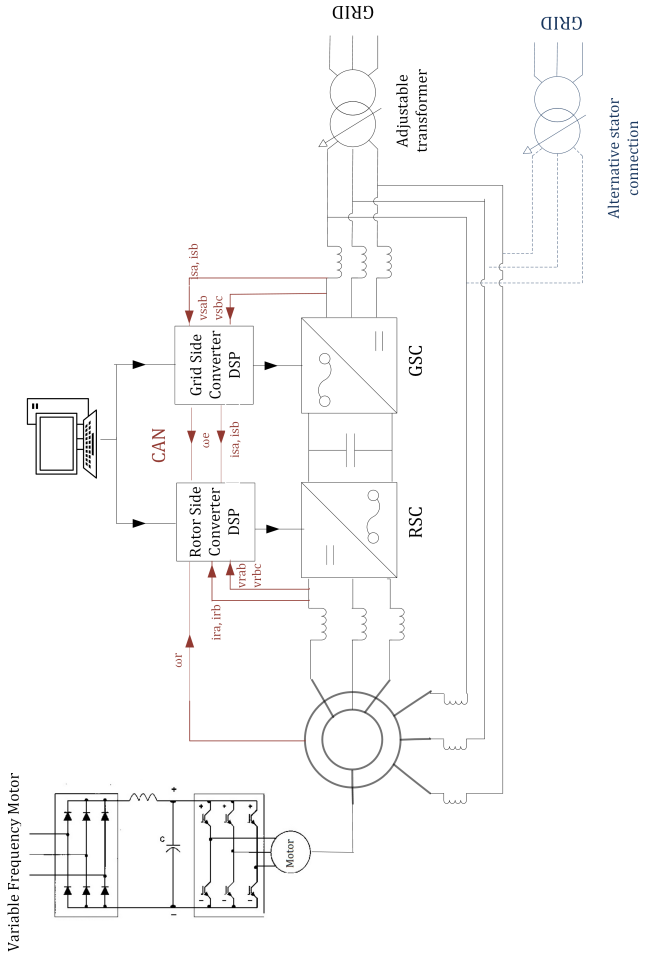

Figure 5.2: Schematic of test bench connections and measurements

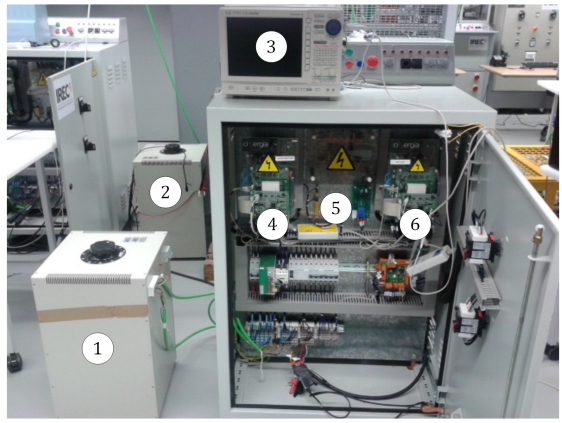

Figure 5.3: Layout of back-to-back converter. 1) Grid-side transformer 2) Stator transformer 3) Oscilloscope 4) Grid-side converter 5) DC bus-bar 6) Rotor-side converter

5.1 Wind profile adapted to test bench

The turbine modeling must be designed to represent a small-scale turbine with a power output equal to the generator used on the test bench. The c_1 to c_7 coefficients are modified to match a real wind turbine with the same rated power. Table 5.1 gathers data from similar wind turbines available on the market. From the characteristics of existing wind turbines, the parameters used in simulation were selected:

Company	P_r (kW)	V_r (m/s)	ω_r (rad/s)	*Radius* (m)
Hannevind	5.5	9	-	3
Antaris	5.5	13	40.8	2.2
Endurance	5.4	11	17.38	3.185
Jetstream3	5.5	12	-	2.5
Taisei	5.5	12	-	3
Eoltec	6	11.5	25.65	2.8
Proven	6	12	20.94*	2.75
Iskra	5	11	20.94*	2.7
QuietRevolution	6	12.5	-	1.55

Table 5.1: Parameters of WTGS available commercially (* Direct Drive)

Radius (m)	ω_r (rad/s)	V_r (m/s)	P_r (kW)
2.07	26	11	5.5

Table 5.2: Turbine parameters used for simulation

The wind profile was then empirically adjusted to match this data by assuming that $CP_{max} = 0.441$ at rated conditions. Table 5.3 shows the final values of the C_p coefficients. Since the test bench generator has 2 pole pairs, the synchronous frequency is 1500 rpm. Thus, by assuming a rated slip of -0.167, the rated shaft speed is set to 1750 rpm and the gearbox ratio of 7.0853.

c_1	c_2	c_3	c_4	c_5	c_6	c_7	c_8	c_9
0.1145	151	0.58	0.0002	2.14	13.2	7.5	-0.02	-0.003

Table 5.3: Wind profile parameters determined empirically

5.2 Control implementation on grid side converter

The code implementation on the GSC was a relatively straight forward process since all the variables required for the calculations were already measured by the B2B converter setup. A probe calibration was necessary to ensure adequate current and voltage readings. It was also found that the switching frequency of each converter should be set to different values in order to avoid interference between them. Frequencies of 12kHz and 24kHz were used on the RSC and the GSC respectively.

Figures 5.4 shows the response to a step input of E_{DC} as measured experimentally and during simulation. The experimental measurements curve is more noisy than the simulation since the latter does not consider the IGBT switching effect but the overall shape of both curves are very similar.

Figure 5.5 presents the response to a direct-axis current step input. The current i_{dr} dictates the reactive power flowing in the rotor circuit. As seen, the measurements follow very well the change of reference value.

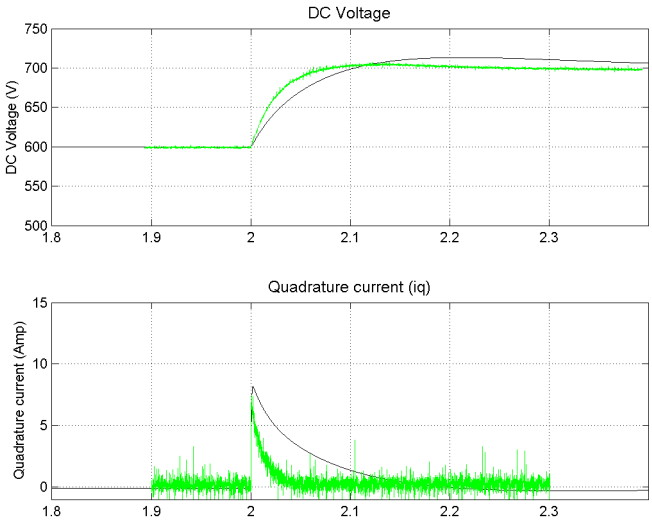

Figure 5.4: Grid Side Converter response to step input of DC bus voltage (E_{DC}). Simulation (black) and Test bench (green)

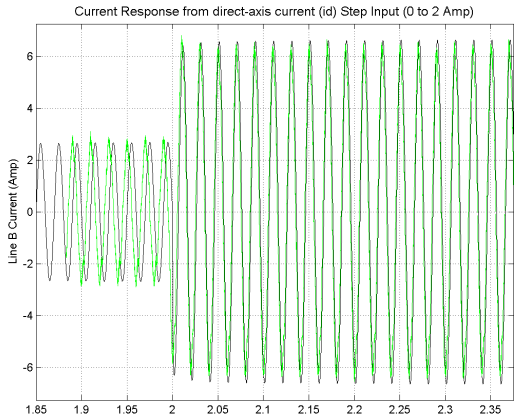

Figure 5.5: Grid Side Converter response to step input of direct-axis current (i_d) from 0 to 2 Amps. Simulation (black) and Test bench (green)

5.2.1 Signal stability

Considerations about the phase lock loop (PLL)

The phase lock loop (PLL) is the tool responsible of computing the frequency and phase angle of the stator voltage. It outputs a signal θ_e with the same frequency as its input signal V_s. Its stability is crucial for a good operation of the system since the stator voltage angle is used in the Park transform. An excessive variation of the PLL's output creates an oscillation of the V_{sd} and V_{sq} signals and of the related signals. Therefore, the PLL control parameters $K_{p,PLL}$ and $K_{i,PLL}$ must be properly selected. Trial and error was used to identify the optimal control parameters:

- $K_p = 1.0$
- $K_i = 1.0$

A smaller value of $K_{p,PLL}$ generally leads to smaller oscillations but the effect is negligible for values lower than approximately 0.1.

Grid side impedance

In the original B2B converter, extra inductances were installed at the ouput of each converter in order to smooth the current output ripple due to the IGBT switching. However, this strongly affects the shape of the current waveform during measurements. By removing the extra inductance installed on the 3-phase side of the RSC, it is possible to obtain better readings. It is also advisable to remove the extra transformer already installed in the B2B converter since a variable transformer is already used for connection to the grid.

5.3 Control implementation on rotor side converter

Due to mal-functionment of the position encoder, it was impossible to operate the RSC correctly in the required timeframe. Different algorithms were tested but due to the absence of a reliable signal of the rotor position, a proper implementation could not be done. This sections summarizes the main points that were adressed while working on the RSC.

5.3.1 Variable measurement in RSC

The rotor variable transformation occuring in the RSC is complex since it deals with two dynamic reference frames rotating at different speeds. In

practice, the computation of constant values in the d-q reference frame requires good instrument calibration, a well-designed stator voltage PLL and accurate rotor angle reading. The presence of oscillation in one single variable can be problematic. The following table lists the different inputs required in the RSC:

Variable	How it is obtained
Stator and rotor voltage and currents (Iab, Ibc, Vab and Vbc)	Probe mounted on each converter
Grid angle (θ_e)	PLL in GSC
Rotor electrical angle (θ_r)	Generator mounted encoder OR Sensorless approach
Alignment angle (δ)	Calculate flux and determine components λ_{sq} and λ_{sd}

Table 5.4: Variables required in rotor-side converter

Where δ is the angle by which the rotor reference frame must be rotated to get variables in d-q aligned with the control frame.

5.3.2 Considerations about the controller area network (CAN)

The CAN is a rapid and relatively reliable way to send data between the RSC and the GSC. However, the DSP processing frequency limits the amount of information that can be sent. In practice, with a switching frequency ($f_{PWM1} = 1/T_{PWM1}$) between 8 and 24 kHz and a CAN speed of 500 kbit/s, the maximal number of variables that could be sent through the CAN is four.

Also, it is advisable to use θ_e, the output of the stator voltage PLL implemented in the GSC, as an input in the RSC. Doing so, instead of sending V_{sa}, V_{sb} and V_{sc} through the CAN, only the value of the stator voltage angle θ_e is transmitted. In the remaining three channels, different variables can be sent, depending on the orientation of the control reference frame and the reference current calculation : $V_{sq}, V_{sd}, P_{rotor}$ Q_{rotor}, i_{sq}, i_{sd}, i_{sa} or i_{sb}.

5.3.3 Different control approach for VOC

One of the control approaches tested on the test bench RSC differs slightly from the one used in the simulation. However, the RSC output voltage

should not be affected since only the calculation method of the reference current differs. This approach is based on the power balance equation presented in [21]. The rotor reference currents are determined from the stator active and reactive power as well as the stator voltage:

$$i_{rd}* = -\frac{P_s^*}{V_s}\frac{X_s}{X_m} \tag{5.1}$$

$$i_{rq}* = -\frac{Q_s^*}{V_s}\frac{X_s}{X_m} - \frac{V_s}{Xm} \tag{5.2}$$

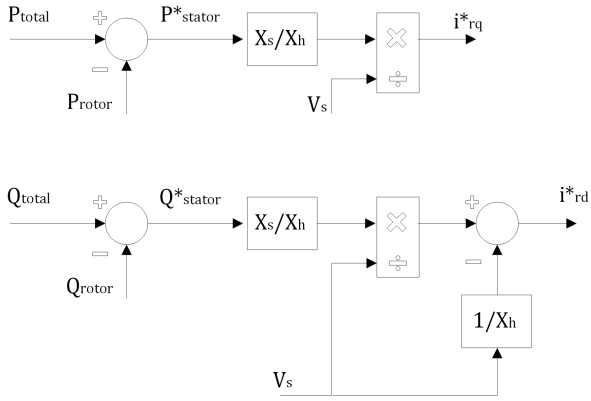

Figure 5.6: Alternative reference current calculations in test bench RSC

Since the GSC already measures the voltage and current of the rotor circuit on its AC side, it can compute the rotor circuit active and reactive power. The CAN is used to transmit these values to the RSC where the reference value of the total active power is computed from the machine speed.

5.4 Voltage ratio consideration

Once the value of the RSC reference voltage has been calculated, it must be divided by the voltage ratio between rotor (V_r) and stator (V_s). The turn ratio (γ) is a constant value equal to the ratio between the number of stator windings and the number of rotor windings. However, the voltage ratio depends on the generator connection scheme. In a $\triangle - Y$ connection,

the grid line voltage is connected to the phase-phase voltage of the primary windings. During testing, this connection was changed to Y-Y configuration, setting the primary winding voltage to a lower value, as shown on Figure 5.7.

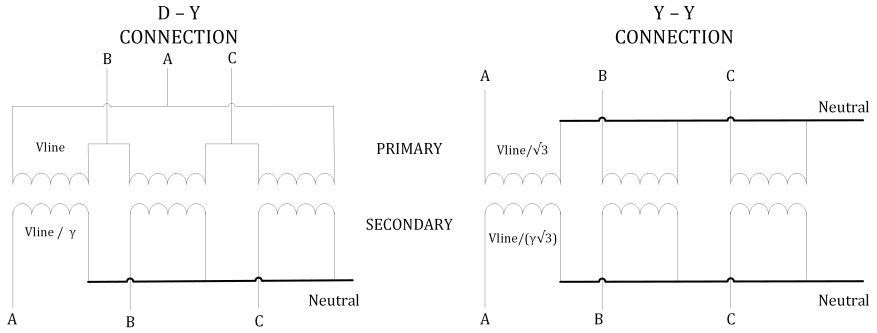

Figure 5.7: Generator connection scheme: $\triangle - Y$ and $Y - Y$

For a generator with $\gamma = 1$, if a Y-Y configuration is used:

$$V_{L,Secondary} = V_{L,Primary} \tag{5.3}$$

In $\triangle - Y$ Configuration

$$V_{L,Secondary} = V_{L,Primary}\sqrt{3} \tag{5.4}$$

Now, using the test bench values of primary line voltage $V_{L,Primary} = 400V$ and turn ratio $\gamma = 3.92$:

In a $\triangle - Y$ configuration, voltage ratio $= 400/(102 \cdot \sqrt{3}) = 2.26$

In a Y-Y configuration, voltage ratio $= 400/102 = 3.92$

Hence, the generator voltage ratio increases by a value of $\sqrt{3}$ when $\gamma > 1$ and the connection is changed from $\triangle - Y$ to $Y - Y$.

5.5 Variable Frequency Motor Drive

A Emerson variable frequency drive performs the speed control of the wind emulating motor. The CTSoft software supplied by the drive manufacturer is used to program the drive from a PC.

Figure 5.8: Variable frequency drive of wind emulating motor

The following values are used in CTSoft for the drive activation:

- Parameters 1.18: enter value of desired generator speed
- Parameters 1.06: enter value of maximal generator speed
- Parameters 6.34: enter ON to start rotation
- Parameters 6.33: enter ON to change drive direction

6 Conclusions

A wind turbine generation system was presented and the modelling of its sub-systems was described. The equations regulating the behavior of internal generator variables and of its connection to the grid were introduced. A voltage oriented control and a stator flux oriented control were developed for the rotor-side converter and a standard approach was presented to control the grid-side converter. A sensorless approach used to obtain the rotor position was described, showing relatively unstable response to input variation, due to the presence of several PI controllers.

The control algorithms were implemented on the B2B converter of a wind turbine test bench. Simulations were performed using realistic perturbances and the results of the GSC response were compared to experimental test bench measurements, showing great similarities. The RSC algorithm was loaded on the converter but problems with the rotor position encoder signal prevented the testing of the complete system behavior.

The next step in this project is the fine-tuning of the sensorless control parameters or the selection of a different sensorless approach. The control can then be implemented on the RSC and experimental results obtained for the complete system behavior. Once the complete test bench is operational, it can be tested with input variations similar to the one used in simulation. An important task to perform then is the verification of the simplifications made in the reference current calculations. Alternatively, an optical position encoder can be installed to measure the rotor position.

Bibliography

[1] Thomas Ackermann. *Wind Power in Power Systems*. Wiley, 2005. 7

[2] M. de Prada. Modelizacion dinamica y control de un aerogenerador de velocidad variable con una maquina de induccion doblemente alimentada en pss.

[3] F. Diaz-Gonzalez. Frequency control support by wind power plants - technical report, December 2012.

[4] F. Diaz-Gonzalez and Andreas Sumper. Modeling, control and experimental validation of a flywheel-based energy storage device. *EPE Journal*, 2012. 31

[5] I. Erlich and J. Kretschmann. Modeling of wind turbines based on doubly-fed induction generators for power system stability studies. *IEEE*, 2008.

[6] EWEA. Creating the internal energy market in europe - technical report. `http://www.ewea.org/fileadmin/files/library/publications/reports/Internal_energy_market.pdf`. I

[7] EWEA. The european wind initiative - wind power research and development to 2020 - technical report. `http://www.ewea.org/fileadmin/files/library/publications/reports/EWI_2013.pdf`. I

[8] Kyriakos Gogas. Design of a robust speed and position sensorless decoupled p-q controlled doubly-fed induction generator for variable speed wind energy applications. 33

[9] O. Gomis-Bellmunt and A. Junyent-Ferre. Ride-through control of a doubly fed induction generator under unbalanced voltage sags. *IEEE transaction on energy conversion*, 23:1036–1045, 2008.

[10] L. Harnefors and Hans-Peter Nee. Model-based current control of ac machines using the internal model control method. *IEEE Transactions on industry applications*, 133-141, 1998.

[11] A Junyent-Ferre. Modelitzacio i control d'un sistema de generacio electrica de turbina de vent.

[12] A. Junyent-Ferre and O. Gomis-Bellmunt. Modeling and control of the doubly fed induction generator wind turbine. *Elsevier*, 23:1036–1045, 2010.

[13] M. Kazmierkowski and F. Blaabjerg. *Control in Power Electronics.* 2002.

[14] GD. Marques and D. Sousa. A dfig sensorless method for direct estimation of slip position. *IEEE*, 2010. 33

[15] T. Neumann and C. Feltes. Development of an experimental rig for doubly-fed induction generator based wind turbine. *Modern Electric Power Systems*, 2010.

[16] Chee-Mun Ong. *Dynamic Simulation of Electrical Machinery.* Prentice Hall PTR, 1998. 12

[17] R. Pena and JC. Clare. Doubly fed induction generator uising back-to-back pwm converters and its application to variables peed wind-energy generation. *IEE*, 1996.

[18] F. Perez Diez and J. Lopez Martinez. *L'energia Minieolica - L'aprofitament local del vent.* Collegi d'enginyers Tecnics Industrials de Barcelona, 2010.

[19] Baike Shen and Bakari Mwinyiwiwa. Sensorless maximum power point tracking of wind by dfig using rotor position phase lock loop (pll). *IEEE Transactions on Power Electronics*, 24:942–951, 2009. 33

[20] Baike Shen and Boon-Teck Ooi. Novel sensorless decoupled p-q control of doubly-fed induction generator (dfig) based on phase locking to y-d frame. *IEEE*, 2005. 33

[21] M. Suwan and T. Neumann. Educational experimental rig for doubly-fed induction generator based wind turbine. *IEEE*, 2012. 58

[22] Vijay Vittal and James McCalley. Impact of increased dfig wind penetration on power systems and markets. `http://repository.asu.edu/attachments/56219/content/Gautam_asu_0010E_10188.pdf`, October 2009. II

[23] B. Wu, Y. Lang, N. Zargari, and S. Kouro. *Power Conversion and Control of Wind Energy Systems*. John Wiley & Sons, 2011. 3, 10, 25

[24] Longya Xu and Wei Cheng. Torque and reactive power control of a doubly fed induction machine by position sensorless scheme. *IEEE Transactions on Power Electronics*, 31:636–642, 1995. 33

A

Test Bench Generator Data

Parameter	Value	Parameter	Value
Company	VEM	$R1(T_{oper})$	3.1
Motor type	SPER 132 SX4	$R1$ (T=20C)	2.4279
Serial Number	18534003	$R^{'}2(T_{oper})$	2.153
Power rating (kW)	5.5	$R2$ (T=20)	0.1081
Frequency (Hz)	50	$Xs1$	3.871
Design speed (rpm)	1450	$X^{'}s2$	4.841
Voltage	400/690	Xm	118.25
Current	11.5/6.8		
Rotor voltage (V)	170		
Rotor current (Amp)	20		
Moment of inertia (kgm^2)	0.05		

Table A.1: Test bench generator data

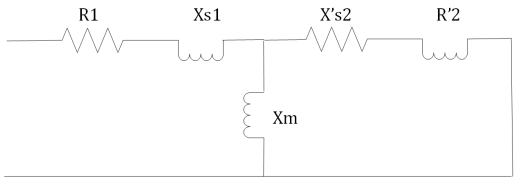

Figure A.1: SCIG simplified electrical schematic

B

Park and Clark Transform

The variables entering the converters are oscillating by nature, which complicates their direct use in the control algorithms. Two techniques known as the Park and Clark transforms are frequently used in electrical machine control because they allow the transformation of time dependant variables into constant values. The mathematical transform depends on the selected orientation of the reference frame, shown on Figure 3.3. They take the following form:

$$\begin{vmatrix} V_\alpha \\ V_\beta \\ V_0 \end{vmatrix} = T_{abc}^{\alpha\beta 0} \begin{vmatrix} V_a \\ V_b \\ V_c \end{vmatrix} \tag{B.1}$$

$$\begin{vmatrix} V_q \\ V_d \\ V_0 \end{vmatrix} = P_{abc}^{qdo} \begin{vmatrix} V_\alpha \\ V_\beta \\ V_0 \end{vmatrix} \tag{B.2}$$

The Clark transform used to change abc into $\alpha\beta$ variables is:

$$T_{abc}^{\alpha\beta 0} = \frac{2}{3} \begin{vmatrix} 1 & -\frac{1}{2} & -\frac{1}{2} \\ 0 & -\frac{\sqrt{3}}{2} & \frac{\sqrt{3}}{2} \\ \frac{1}{2} & \frac{1}{2} & \frac{1}{2} \end{vmatrix} \tag{B.3}$$

The Park transform used to change abc into dqo variables is:

$$P_{abc}^{qdo} = \frac{2}{3} \begin{vmatrix} cos(\theta) & cos(\theta - \frac{2\pi}{3}) & cos(\theta + \frac{2\pi}{3}) \\ sin(\theta) & sin(\theta - \frac{2\pi}{3}) & sin(\theta + \frac{2\pi}{3}) \\ \frac{1}{2} & \frac{1}{2} & \frac{1}{2} \end{vmatrix} \tag{B.4}$$

C

Turn On Procedure

Connection and power up:

- Connect the PC to the variable frequency drive, open the breakers of the unused drives in the (Emerson) cabinet and power the cabinet.
- Connect the stator and the grid side converter to adjustable transformers (or both to the same transformer). Set the transformers to 0 %. Turn On the transformer(s).
- Connect the rotor cables to the RSC
- Connect the encoder mounted on the DFIG generator to the RSC

Code loading and IGBT commutation:

- With adjustable transformer at 0%, *Debug* CodeComposer on both PCs. Enter the *RealMode* in order to view measurement on the sreen and allow variable user input. Press *Run* (green arrow).
- Ensure that RSC code is loaded on the DSP. Enter $enmarxa = 1$. Raise the GSC transformer to 60%. Enter $maquina_estat = run$. The GSC is commutating.
- Increase progressively the DC bus voltage $Easterisc$ to 700 V.
- If the stator is connected to an independant transformer, increase its voltage to 100%.
- In the RSC, enter $enmarxa = 1$. Wait a few seconds, then enter $enmarxapausa = 0$. The RSC is commutating.

D

Simulink blocks of control algorithm

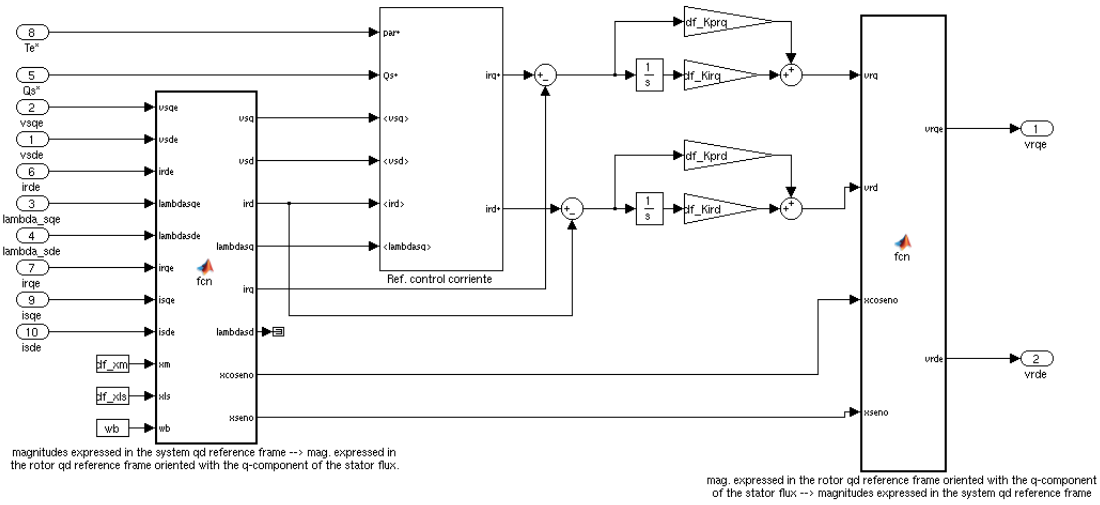

Figure D.1: Overall schematic of flux oriented control algorithm (FOC)

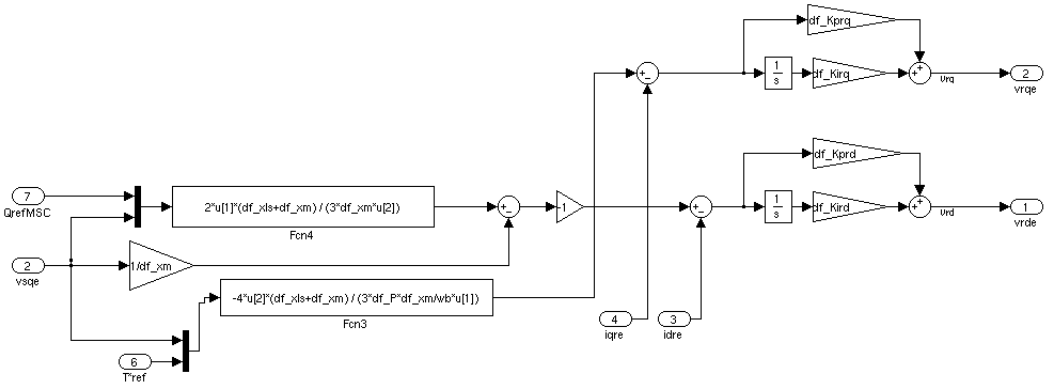

Figure D.2: Overall schematic of voltage oriented control algorithm (FOC)

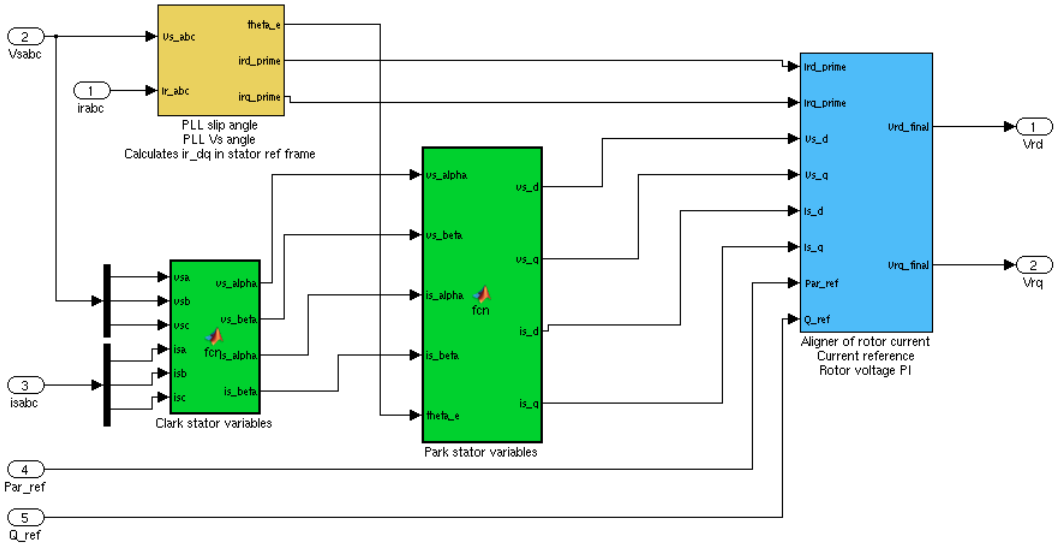

Figure D.3: Overall schematic of sensorless algorithm

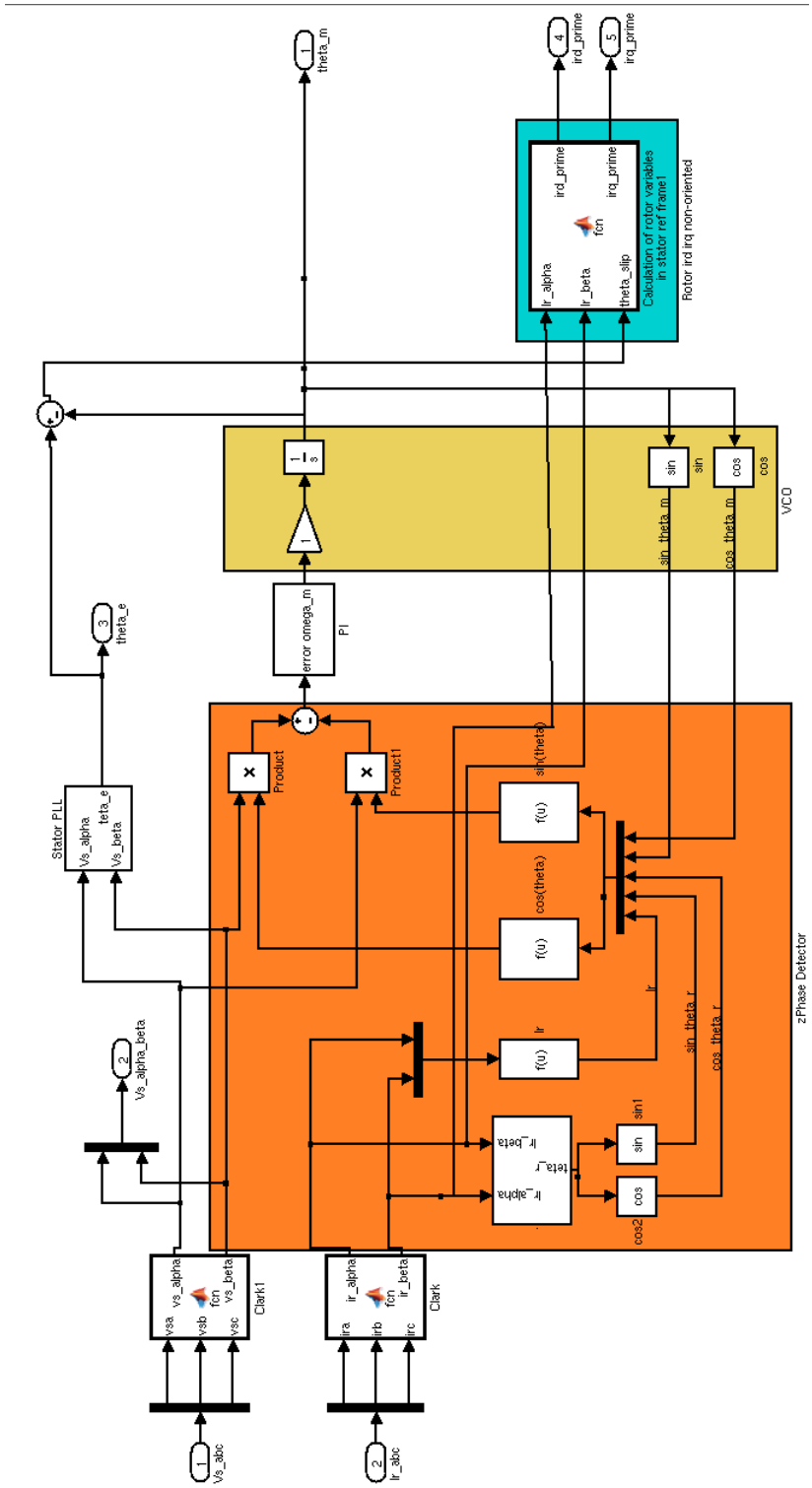

Figure D.4: Schematic of PLL and VCO system used in the sensorless algorithm for calculation of θ_r and θ_e

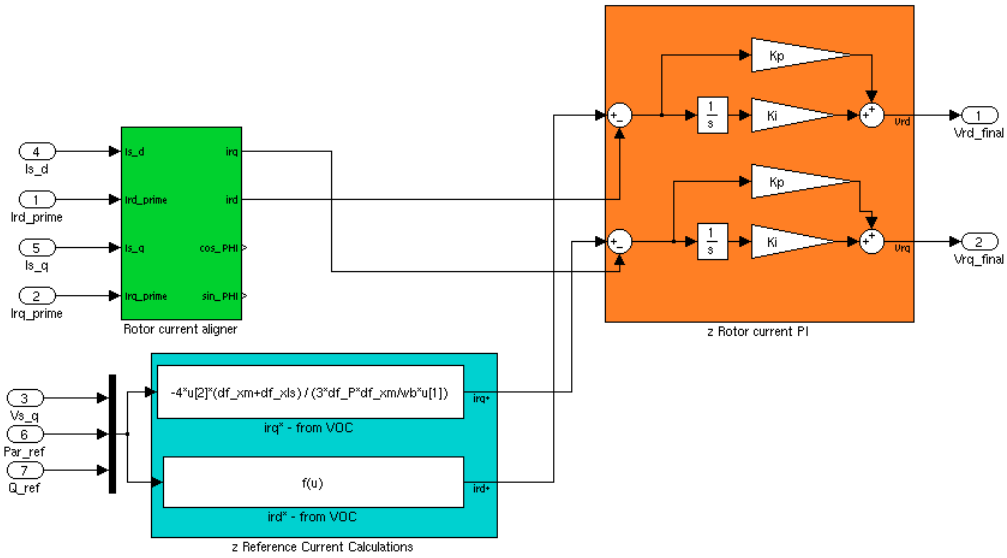

Figure D.5: Schematic of aligner and PI used in the sensorless algorithm

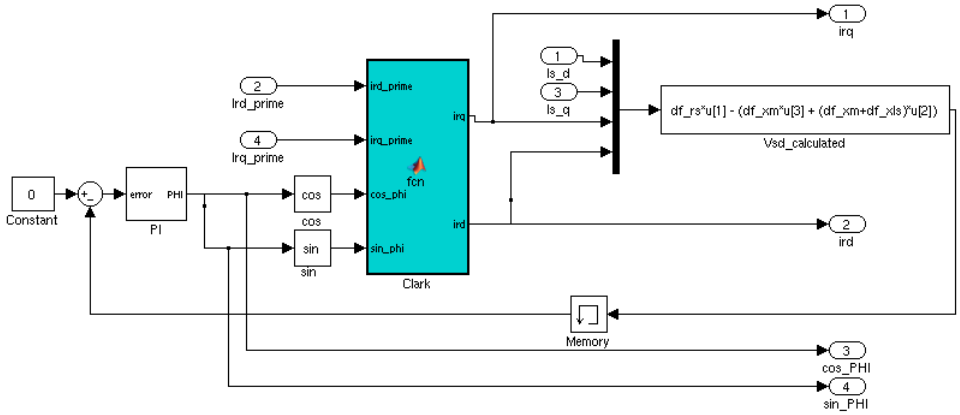

Figure D.6: Aligner sub-block used in the sensorless algorithm